applied sciences

MDPI

Article

Probing Petroleum Sources Using Geochemistry, Multivariate Analysis, and Basin Modeling: A Case Study from the Dibei Gas Field in the Northern Kuqa Foreland Basin, NW China

Xinzhuo Wei [1], Keyu Liu [1,2,*], Xianzhang Yang [3], Jianliang Liu [1,*], Lu Zhou [3] and Xiujian Ding [1]

[1] National Key Laboratory of Deep Oil and Gas, China University of Petroleum, Qingdao 266580, China; xinzhuowei1998@163.com (X.W.); dingxj@upc.edu.cn (X.D.)
[2] Laoshan Laboratory, Qingdao 266071, China
[3] Institute of Petroleum Exploration and Development, Tarim Oilfield Company, PetroChina, Korla 841000, China; yangxz-tlm@petrochina.com.cn (X.Y.); zhoulu-tlm@petrochina.com.cn (L.Z.)
* Correspondence: liukeyu@upc.edu.cn (K.L.); liujianliang@upc.edu.cn (J.L.)

Abstract: The Dibei Gas Field, located in the northern Kuqa Foreland Basin, Tarim Basin, western China, is one of the most important condensate gas-producing areas in China, with over one trillion cubic feet of gas reserves discovered in the Jurassic terrestrial reservoirs. However, further hydrocarbon exploration and development in the area is hampered by uncertainties on the petroleum sources. A robust oil–source and gas-source correlation analysis was carried out in the Dibei area to enhance our understanding of the gas accumulation potential. An integrated molecular geochemical analysis, multivariate analysis, and basin modeling were conducted to investigate source rocks, inclusion oils, reservoir oils, and gas from the Dibei area. Two types of source rocks have been identified in the Dibei area: a Jurassic coaly source rock and a Triassic lacustrine source rock based on multivariate analysis. The compositions of the *n*-alkanes, steranes, and terpanes and the carbon isotope ratios of individual *n*-alkanes in the inclusion oil extracts and reservoir oils from Jurassic Yangxia and Ahe reservoirs show distinct differences when compared with the two types of source extracts. Multiple oil sources are revealed in the Dibei area, with various degrees of mixing between reservoir oil (present) and inclusion oil (paleo), reflecting evolving oil sources. Basin modeling shows that during the late Himalayan orogeny, the Jurassic strata in the Dibei area experienced a rapid burial within ~20 Ma, with the oil generation window of the source rocks expanding greatly. This caused the shallowly buried Jurassic source rocks to enter the oil generation window, resulting in the occurrence of two oil sources for the inclusion oils and reservoir oils, and an increasing degree of mixing over time. Our finding confirms that the accumulated condensate gas in the Dibei area is mainly derived from the Jurassic source rocks. This allows the extent of prospective exploration to be better defined.

Keywords: petroleum geochemistry; oil–source correlation; multivariate analysis; basin modeling; Kuqa Foreland Basin

check for updates

Academic Editor: Nikolaos K. Koukouzas

Received: 6 January 2025
Revised: 17 February 2025
Accepted: 21 February 2025
Published: 24 February 2025

Citation: Wei, X.; Liu, K.; Yang, X.; Liu, J.; Zhou, L.; Ding, X. Probing Petroleum Sources Using Geochemistry, Multivariate Analysis, and Basin Modeling: A Case Study from the Dibei Gas Field in the Northern Kuqa Foreland Basin, NW China. *Appl. Sci.* **2025**, *15*, 2425. https://doi.org/10.3390/app15052425

Copyright: © 2025 by the authors. Licensee MDPI, Basel, Switzerland. This article is an open access article distributed under the terms and conditions of the Creative Commons Attribution (CC BY) license (https://creativecommons.org/licenses/by/4.0/).

1. Introduction

Foreland basins hold over 40% of the world's conventional hydrocarbon resources and are an important field for deep and ultra-deep oil and gas exploration and development [1,2]. However, complex reservoir formation conditions, such as multi-sources [3–5], spatiotemporal differences in sources [6–9], various sedimentary environments [9–11],

heterogeneity of sources and reservoirs [12–14], and the mixing of multi-stage charged reservoir oils [7,15,16], have impeded the prediction of the prospective hydrocarbon accumulation areas. Therefore, clarifying oil–source correlations is crucial to further hydrocarbon exploration and development, especially in structurally active foreland basins.

Advanced organic geochemical methods have been used since the late 1970s for oil–source correlation [17,18]. Source rock pyrolysis parameters, consisting of total organic carbon (TOC), hydrogen index (HI), hydrocarbon generating potential ($S_1 + S_2$), and the highest pyrolysis peak temperature (T_{max}), were generally used for the identification and evaluation of source rocks [10,19], providing insight on the hydrocarbon prospectivity in sedimentary basins. The oil–source correlations have been used to determine if there is a genetic relationship between oils and sources by comparing geochemical data between reservoir oils and source rock extracts. George et al. (1997) [20] developed online and offline fluid inclusion analytical methods termed the Molecular Composition of Inclusions (MCI) methods to obtain extracts of inclusion oils for geochemical analysis. These methods avoid the loss of light hydrocarbon components, contamination, and secondary alterations of the hydrocarbons in the analysis so as to reflect the geochemical information more accurately. The MCI analysis is less able to distinguish the oil inclusions with different fluorescence colors and charge timing in the same sample [21]. Consequently, it is necessary to select the samples with a single type of oil inclusions for MCI analysis. Some studies have shown that the geochemical properties of inclusion oils may sometimes be quite different from those of the associated reservoir oils [22–24]. These differences may reflect changes in reservoir oils over time [25], may be the result of differences in sources [26–28], or may be the result of fractionation in reservoirs [22,29].

In recent years, statistical methods, such as multivariate analysis, have developed rapidly and have been widely applied in the field of organic geochemistry [30–32]. Multivariate analysis can be used to discriminate oils from different types of sources and depositional environments, as well as from different levels of thermal maturity [33–35]. The multivariate statistical approach includes hierarchical clustering analysis (HCA) and principal component analysis (PCA). The combination of conventional organic geochemical analyses and interpretations with statistical analysis provides the most reliable oil–oil and oil–source correlations. Basin and petroleum system modeling (BPSM) is a useful tool for the analysis of hydrocarbon generation, migration, and accumulation, for visualizing hydrocarbon migration pathways and calculating hydrocarbon yields in geological periods [36–39]. This can provide guidance for delineating areas favorable for hydrocarbon accumulation [40–42]. Through 2D basin modeling, the hydrocarbon generation from each set of source rocks during various geological periods can be quantitatively simulated to evaluate and predict the possible sources of oil inclusion extracts (paleo) and reservoir oils (present).

Recent progress has been achieved in the exploration of deep oil and gas resources within the Kuqa Foreland Basin, Tarim Basin, NW China [43]. The Jurassic terrestrial clastic reservoirs are important intervals with the discovery of a series of large- or medium-sized hydrocarbon accumulations in the northern Kuqa Foreland Basin (e.g., YN-2 well, Tudong-2 well, DB-104 well, etc.) [44–46]. Multiple sets of organic-rich lacustrine mudstones and coal measures are present in the Jurassic and Triassic formations, providing sufficient source capacity for large-scale oil and gas accumulations [47–51]. However, uncertainties on the relative contributions of the multi-sources of petroleum have impeded the prediction of the prospective hydrocarbon accumulation areas. Controversial opinions of oil–sources in the northern Kuqa Foreland Basin have centered on the uncertainty of whether the hydrocarbons in the Jurassic reservoirs originated from the Triassic lacustrine source rocks or the Jurassic coaly source rocks by comparing the geochemical data among reservoir oils,

oil sands, and source rocks [44,48,49,52]. For example, Song et al. (2019) [52] proposed that almost all the Jurassic oils were generated from the Jurassic coal measures, with only a minor contribution of the Triassic lacustrine source rocks. Conversely, it has also been proposed that the reservoir oils in the J_1a Formation were mainly generated from the Triassic lacustrine mudstones, while the J_1y reservoir oils were derived from Jurassic coaly source rocks with a slight mixing from the Triassic lacustrine mudstones [44,46].

In this study, systematic molecular geochemical correlations among source rock extracts, oil inclusion extracts, reservoir oils, and gas are carried out to identify the oil–source in the northern Kuqa Foreland Basin. Multivariate analysis (HCA/PCA) and Basin and petroleum system modeling (BPSM) are coupled to validate the traditional biomarkers interpretation, resolving the problem of multiple interpretations of geochemistry data and restoring oil–sources evolution in various geological periods. This offers new insight for oil–source correlations in the northern Kuqa Foreland Basin and in basins with similar geological backgrounds with multi-sources and multi-stage hydrocarbon charges and accumulations.

2. Geological Setting

Kuqa Foreland Basin, as the north part of Tarim Basin, is bordered by the South Tianshan Mountain to the north and linked to the Tabei Uplift and Awati Sag to the south. The Kuqa Foreland Basin is the key productive gas zone of the Tarim Basin, with an exploration area of 28 × 10^3 km^2, 500 km from west to east, and 30–70 km from north to south (Figure 1A) [3]. The Kuqa Foreland Basin contains four tectonic units: the Northern Structural Belt, Kelasu Structural Belt, Qiulitage Structural Belt, and the Southern Structural Belt from north to south [45]. The Northern Structural Belt, located in the northmost region of the Kuqa Foreland Basin, comprises four distinct sub-structural domains: the Northern Slope Belt, the Central Anticline Belt, the Southern Slope Belt, and the Sag Belt (Figure 1B,C). The Dibei Gas Field is the main gas condensate generation zone in the northern Kuqa Foreland Basin (Figure 1B) [44,46,53].

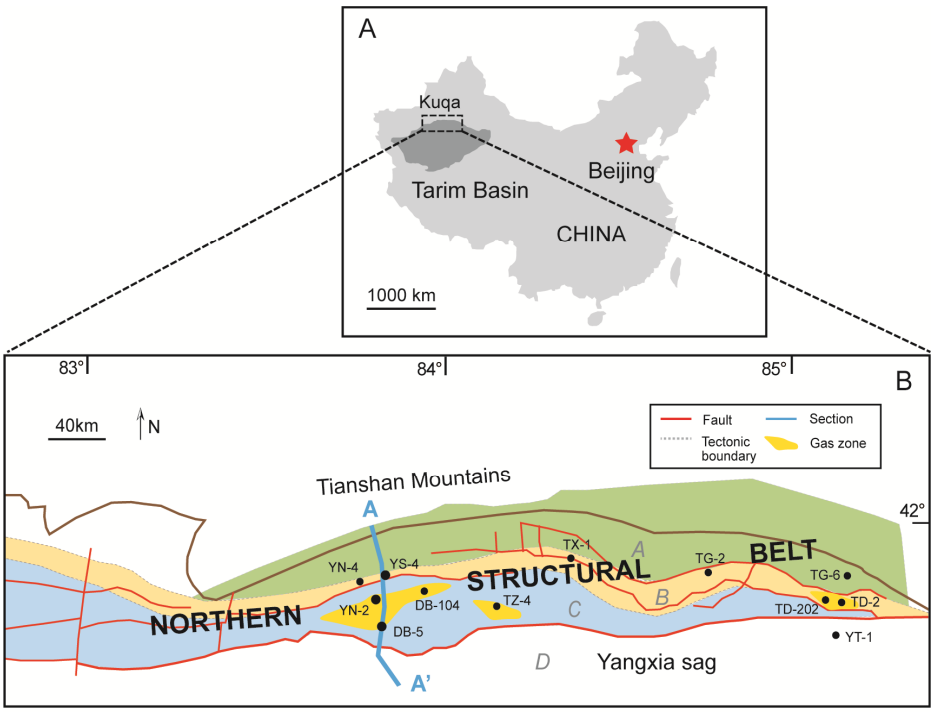

Figure 1. *Cont.*

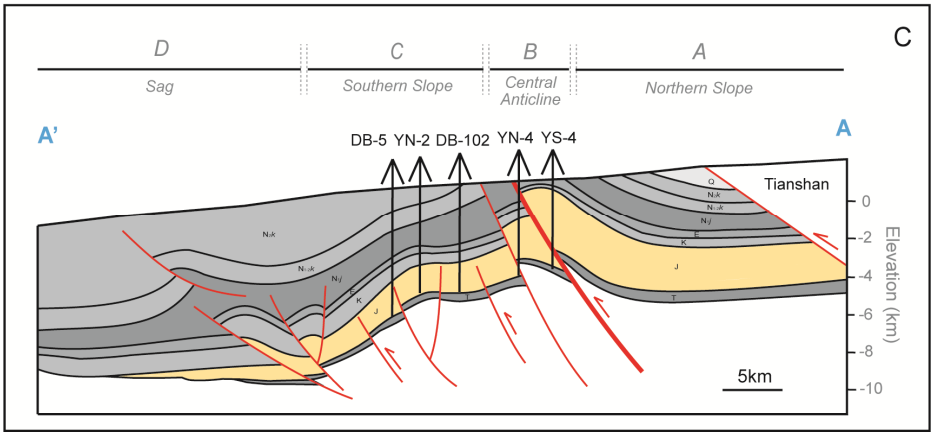

Figure 1. (**A**) Location map of the Kuqa Foreland Basin, Tarim, NW China; (**B**) Structural outline map of the northern Kuqa Foreland Basin showing the distribution of trust faults, gas reservoirs and wells, the boundary of four sub−structural belts, and the position of the N−S cross−section AA′; (**C**) N−S cross−section AA′ of the Kuqa Foreland Basin showing the location of wells in sub−structural belts, the distribution of various thrust faults, and the key stratigraphic intervals. The stratigraphic symbols in the AA′ section are shown in Figure 2.

The three stages of tectonic evolution can be divided in the Kuqa Foreland Basin: a foreland basin stage during the Triassic period, an extensional rift stage in the Jurassic and Cretaceous periods, and a rejuvenated foreland basin stage from the Early Paleogene to the present [54]. Multiple source rocks are developed in the Triassic and Jurassic strata, including the Kezilenuer (J_2kz), Yangxia (J_1y) and Taliqike (T_3t) coal measures source rocks and the Huangshanjie (T_3h) fluvial-lacustrine source rocks (Figure 2) [44,55], with a decreasing maturity from the Yangxia Sag Belt to the Yiqikelike Anticline Belt [4] (Figure 1C). The reservoirs are mainly developed in the Yangxia Formation (J_1y) and Ahe Formation (J_1a), with relatively good reservoir properties (porosity: 2–12%, permeability: 0.01 mD–100 mD) and are adjacent to source rocks (Figure 2). The Jurassic reservoirs are mainly dominated by fine-grained lithic arkose sandstone and siltstone deposited in braided rivers and delta environments [56]. The development of micro-fractures in each sub-structural interval strongly affected the migration of hydrocarbons and formed an effective storage space in deep gas reservoirs [57,58]. The J_2kz and J_1y source rocks acted as excellent regional seals or overlying seals for the preservation of oil and gas accumulated in the Jurassic reservoirs [44,59]. During the late Himalayan orogeny (~23.3 Ma), large amounts of secondary thrust faults were reactivated under the influence of intense tectonic compression in the northern Kuqa Foreland Basin [48,60,61], leading to the rapid burial of source rocks and complex in-reservoir alternation of accumulated oil and gas [44,62,63].

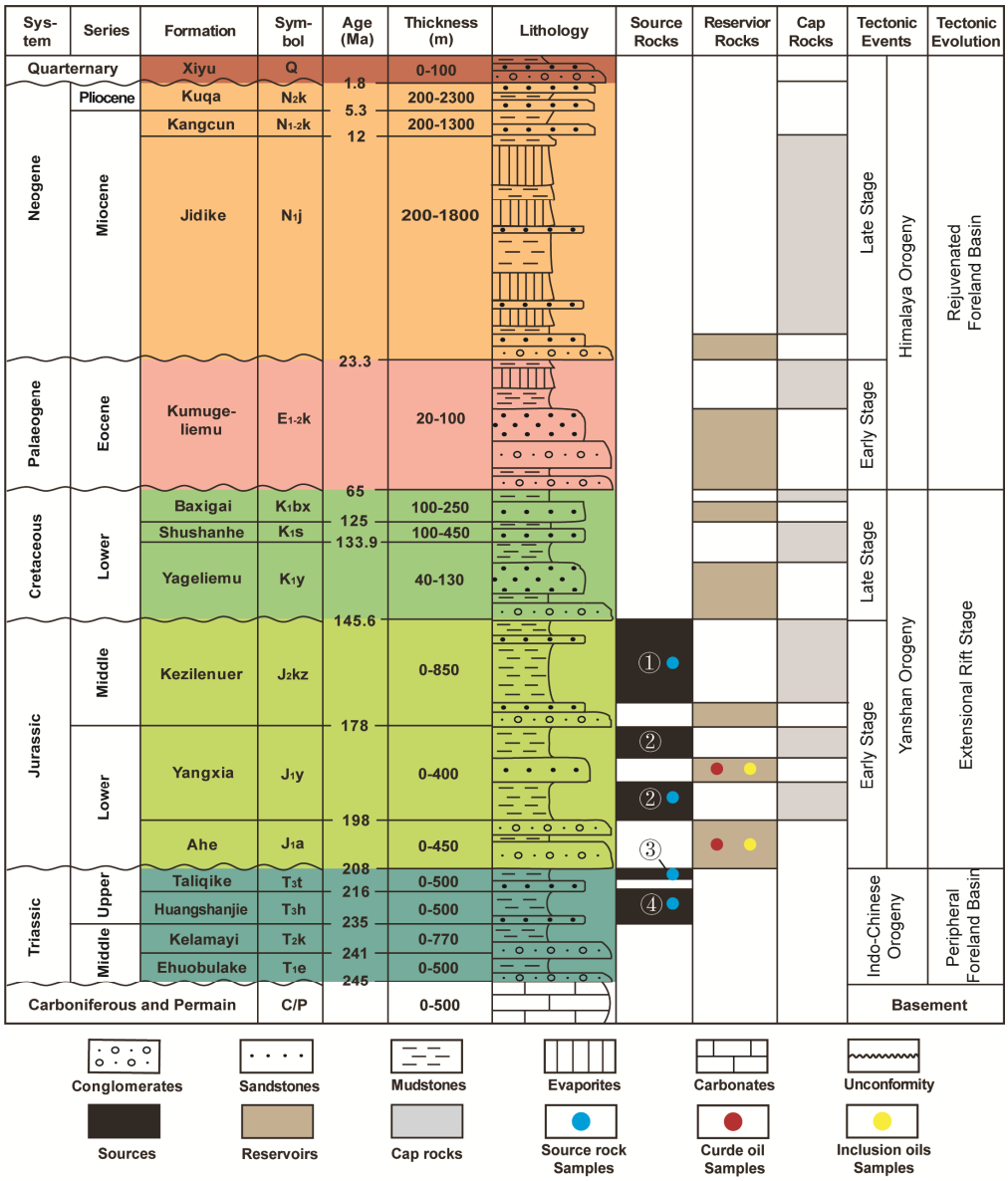

Figure 2. Generalized Paleozoic–Cenozoic stratigraphic map of the northern Kuqa Foreland Basin (modified from Liu et al., 2016 [63]), illustrating tectonic evolution stages and the position of selected samples and major petroleum system elements, including four sets of source rocks, reservoirs, and cap rocks.

3. Samples and Methods

3.1. Sample Preparation

A total of seven source rock samples were selected from four sets of source rocks, including the Triassic Huangshanjie (T_3h) source rocks, Triassic Taliqike (T_3t) source rocks, Jurassic Yangxia (J_1y) source rocks, and Jurassic Kezilenuer (J_2kz) source rocks, with burial depths ranging from 3220.8 m to 5310.0 m. TOC and HI values were provided by the Tarim Oilfield Company, PetroChina (Beijing, China). TOC values were run on the samples as the standard of screening and the selected samples with high TOC values are shown in Table 1. A total of five reservoir oil samples were selected from the Jurassic reservoirs (J_1y and J_1a Formation) in the Dibei area (Table 1, data were provided by the Tarim Oilfield, PetroChina). A total of eight core samples with high values of Grains containing Oil Inclusions (GOIs) from the J_1y Formation and J_1a Formation were selected from the oil-bearing rocks [64,65], which were dominated by almost the same type of oil inclusions assemblage (OIA) [66]. The

proportions of two types of oil inclusion assemblages (OIAs) containing dominantly yellow fluorescing color or dominantly blue fluorescing color in the same sample are shown in Table 1. The stable carbon isotope data of gas are provided from Tarim Oilfield, PetroChina.

Table 1. Samples used for geochemistry analysis.

No.		Well	Type	Formation	Depth/m	Proportion Oil Inclusion (Yellow:Blue)		GOI/%
1	Source-1	YN-2	Source rock	J_2kz	4319.8	/		/
2	Source-2	YN-4	Source rock	J_2kz	3220.8	/		/
3	Source-3	YN-2	Source rock	J_1y	4439.5	/		/
4	Source-4	YN-4	Source rock	J_1y	4230.1	/		/
5	Source-5	YN-2	Source rock	T_3t	5003.0	/		/
6	Source-6	YN-2	Source rock	T_3h	5310.0	/		/
7	Source-7	YN-2	Source rock	T_3h	5318.0	/		/
8	Oil-1	YN-2	Crude oil	J_1y	4746.0	/		/
9	Oil-2	YN-2	Crude oil	J_1y	4776.0	/		/
10	Oil-3	YN-2	Crude oil	J_1y	4905.0	/		/
11	Oil-4	DB-104	Crude oil	J_1a	4768.0	/		/
12	Oil-5	DX-1	Crude oil	J_1a	4800.0	/		/
13	Inclusion-1	YN-2	Oil inclusion	J_1y-B	4547.6	19:81	Blue sample	42.7
14	Inclusion-2	YS-4	Oil inclusion	J_1y-Y	2585.5	89:11	Yellow sample	46.9
15	Inclusion-3	DB-5	Oil inclusion	J_1a-B	5842.2	0:100	Blue sample	69.2
16	Inclusion-4	DB-5	Oil inclusion	J_1a-B	5844.4	0:100	Blue sample	67.0
17	Inclusion-5	DB-102	Oil inclusion	J_1a-B	4980.5	0:100	Blue sample	45.6
18	Inclusion-6	DB-102	Oil inclusion	J_1a-B	5033.8	0:100	Blue sample	62.0
19	Inclusion-7	YS-4	Oil inclusion	J_1a-Y	4005.0	98:2	Yellow sample	45.0
20	Inclusion-8	YS-4	Oil inclusion	J_1a-Y	4072.6	90:10	Yellow sample	21.4

Crushed core samples were cleaned sequentially to obtain extracts of the source rocks and inclusion oils following the procedure proposed by Liu et al. (2014) [67]. Following the standards of Molecular Composition of Inclusion (MCI) protocols [20,68], the extraction of the inclusion oils, reservoir oils, and source rock extracts was tested by gas chromatography–mass spectrometry (GC–MS) analysis. The extracts of oils were quantitatively fractionated into saturated hydrocarbon, aromatic hydrocarbon, resin, and asphaltene (SARA), and 5α androstane and deuterated monadamantane (AD16) were used as analytical standards. The saturated hydrocarbon, aromatic hydrocarbon, and resins were rinsed with *n*-hexane, dichloromethane/*n*-hexane (2:1), and methanol (10% dichloromethane), respectively. Before the separation of the four groups of factions, asphaltene was first precipitated using 40-fold concentrated *n*-hexane as the solvent. The filtrate was concentrated to a volume of approximately 1 mL by rotary evaporation. Resins and asphaltene were weighted, and saturated and aromatic hydrocarbons were weighed after the GC–MS analysis. Gas chromatography (GC) analysis of the source rock extracts and oil extracts was performed using an Agilent 7890B GC instrument fitted with an HP-5 column, a 30 m $\times$ 0.32 mm i.d., 0.25 µm film thickness, and nitrogen with a constant flow was used as the carrier gas. After GC analysis, saturated hydrocarbon was separated into *n*-, *iso*-, and *cyclo*-alkanes using urea as the complexing agent. GC–MS analysis of *iso*- and *cyclic*-alkanes was performed using an Agilent 5975B/6890N GC–MSD equipped with an HP-5MS column with 30 m $\times$ 0.25 mm i.d., 0.25 µm film thickness. Terpanes and steranes were quantified on m/z 191 and m/z 217 mass chromatograms using internal 5α androstane as a standard. Aromatic components were analyzed using an Agilent 5975B/6890N GC–MSD equipped with an HP-5MS column with 60 m $\times$ 0.25 mm i.d., 0.25 µm film thickness. Aromatic fractions were quantified on m/z 50–550 chromatograms using dibenzothiophene-d8 as an internal standard. The carbon isotope compositions of individual *n*-alkanes were analyzed using the GV IsoPrime GC-IRMS (Agilent-6890-Isoprim (Agilent, Santa Clara, CA, USA))

instrument with a spitless and constant flow. The ratios of the biomarkers were calculated based on the area of peaks. GC–MS analysis was performed at the Guangzhou Institute of Geochemistry, Guangzhou, China and the instruments were manufactured by Agilent Technologies, Santa Clara, CA, USA.

3.2. Multivariate Statistical Analysis

3.2.1. Hierarchical Clustering Analysis (HCA)

Hierarchical cluster analysis (HCA) is one of multivariate statistical techniques that has been successfully used in oil–source correlations [30–32]. HCA uses the Ward method to calculate the sum of the total variance and the mean values of clusters through the squared Euclidean distance formula, so as to evaluate the membership of clusters. In geological applications, the cluster distance between oil samples and source rock samples is calculated by n-dimensional space, in which n represents the number of selected component parameters. The SPSS Statistics (version 27) developed by IBM was used for the statistical analysis. The study used 11 geochemical parameters from 17 target samples for HCA analysis (Table 2).

Table 2. Selected molecular parameters and ratios derived from isoprenoids, steranes, terpanes and aromatic components.

	No.	Well	Formation	R1 *	R2	R3 *	R4 *	R5 *	R6 *	R7 *	R8 *	R9 *	R10 *	R11 *	R12 *	R13	R14	R15	R16	R17
1	Source-1	YN-2	J_2kz	0.22	0.11	0.68	0.32	1.87	0.66	0.32	0.36	0.26	0.12	0.46	0.43	/	/	/	/	/
2	Source-2	YN-4	J_2kz	0.17	0.14	0.69	0.25	4.89	0.55	0.12	0.22	0.18	0.21	0.42	0.47	0.46	0.26	0.93	0.84	1.22
3	Source-3	YN-2	J_1y	0.24	0.19	0.57	0.42	0.87	0.24	0.23	0.44	0.31	0.14	0.39	0.41	/	/	/	/	/
4	Source-4	YN-4	J_1y	0.37	0.08	0.55	0.66	1.87	0.79	0.36	0.83	0.45	0.24	0.48	0.35	0.47	0.30	0.95	0.97	1.18
5	Source-5	YN-2	T_3t	0.23	0.20	0.56	0.41	2.90	0.30	0.11	0.93	0.48	0.26	0.52	0.38	0.49	0.27	1.01	0.87	1.17
6	Source-6	YN-2	T_3h	0.33	0.19	0.48	0.68	0.80	0.42	0.21	0.94	0.52	0.24	0.75	0.48	0.61	0.34	1.32	1.10	1.10
7	Source-7	YN-2	T_3h	0.28	0.26	0.46	0.62	0.85	0.43	0.25	1.05	0.51	0.25	0.89	0.45	/	/	/	/	/
8	Oil-1	YN-2	J_1y	0.27	0.27	0.46	0.58	2.04	0.21	0.09	0.69	0.41	0.17	0.51	0.48	/	/	/	/	/
9	Oil-2	YN-2	J_1y	0.30	0.16	0.54	0.54	1.94	0.21	0.10	1.27	0.56	0.27	0.59	0.53	/	/	/	/	/
10	Oil-3	YN-2	J_1y	0.33	0.20	0.47	0.70	1.88	0.24	0.11	1.05	0.51	0.19	0.62	0.45	/	/	/	/	/
11	Oil-4	DB-104	J_1a	0.43	0.17	0.39	1.10	1.04	0.10	0.07	1.73	0.73	0.21	0.50	0.43	/	/	/	/	/
12	Oil-5	DX-1	J_1a	0.43	0.20	0.37	1.16	2.62	0.23	0.08	1.57	0.61	0.19	0.59	0.48	/	/	/	/	/
13	Inclusion-1	YN-2	J_1y-B	0.23	0.18	0.59	0.38	0.63	0.33	0.12	1.21	0.55	0.15	0.67	0.39	0.64	0.27	1.38	0.88	0.16
14	Inclusion-2	YS-4	J_1y-Y	0.24	0.18	0.58	0.41	0.41	0.27	0.12	1.04	0.52	0.15	0.64	0.47	0.53	0.27	1.11	0.87	0.24
15	Inclusion-3	DB-5	J_1a-B	0.38	0.12	0.50	0.75	1.07	0.43	0.34	1.24	0.55	0.19	0.43	0.30	/	/	/	/	0.93
16	Inclusion-4	DB-5	J_1a-B	0.35	0.22	0.43	0.82	1.04	0.26	0.20	1.21	0.55	0.30	0.45	0.48	/	/	/	/	0.93
17	Inclusion-5	DB-102	J_1a-B	0.40	0.24	0.35	1.13	1.23	0.48	0.34	1.38	0.58	0.26	0.43	0.37	/	/	/	/	0.96
18	Inclusion-6	DB-102	J_1a-B	0.33	0.40	0.26	1.26	1.51	0.41	0.30	1.36	0.58	0.22	0.48	0.42	0.54	0.32	1.13	1.05	0.71
19	Inclusion-7	YS-4	J_1a-Y	0.30	0.24	0.45	0.68	1.04	0.43	0.59	1.29	0.56	0.14	0.38	0.39	0.49	0.29	1.00	0.95	0.92
20	Inclusion-8	YS-4	J_1a-Y	0.33	0.14	0.53	0.63	0.76	0.39	0.43	1.33	0.57	0.15	0.41	0.34	0.50	0.31	1.03	1.00	0.87

Note: R1, $C_{27}/(C_{27} + C_{28} + C_{29})\alpha\alpha\alpha$ 20R sterane; R2, $C_{28}/(C_{27} + C_{28} + C_{29})\alpha\alpha\alpha$ 20R sterane; R3, $C_{29}/(C_{27} + C_{28} + C_{29})\alpha\alpha\alpha$ 20R sterane; R4, C_{27}/C_{29} $\alpha\alpha\alpha$ 20R sterane; R5, Pr/Ph; R6, Pr/n-C_{17}; R7, Ph/n-C_{18}; R8, Ts/Tm; R9, Ts/(Ts + Tm); R10, Gammacerane/C_{30} hopane; R11, C_{29} $\beta\beta/(\alpha\alpha + \beta\beta)$ sterane; R12, C_{29} $\alpha\alpha\alpha$ 20S/20(R + S) sterane; R13, F_1 = (2-MP + 3-MP)/(1-MP + 2-MP + 3-MP + 9-MP); R14, F_2 = 2-MP/(1-MP + 2-MP + 3-MP + 9-MP); R15, Ro-F_1 = $2.598F_1 - 0.27494$; R16, Ro-F_2 = $3.932F_2 - 0.01236$; R17, CPI = $1/2[(\sum C_{25} - C_{33}/\sum C_{24} - C_{32}) + (\sum C_{25} - C_{33}/\sum C_{26} - C_{34})]$. MP: methylphenanthrene. Symbol * is the parameter used in HCA and PCA analysis.

3.2.2. Principal Component Analysis (PCA)

Principal component analysis (PCA) is another powerful multivariate statistical technique used to extract the linear relationships of the original variables. By transforming the original variables into their linear combinations (principal component, PC), dimensionality reduction is achieved while retaining important information. Varimax rotation was applied to enhance the interpretability of principal components (PCs) by maximizing the variance of their loadings. This was achieved by reducing the number of both high and low coefficients, thereby increasing the contrast between them [69,70]. When the original variables are transformed linearly by varimax rotation, the obtained PCs after dimensionality reduction can effectively preserve the features of the original variables, among which those with the largest proportion of variance have the strongest ability to reflect the original variables [17,18,71]. In the PCA results, the original data matrix was decomposed into two

components: the score matrix, which represents the projections of the data onto the PCs, and the loading matrix, which indicates the contribution of each original variable to the principal components. The data in Table 2 were used for PCA analysis.

3.3. Basin and Petroleum System Modeling (BPMS)

Two-dimensional basin and petroleum system modeling (BPSM) was performed using PetroMod® software (version 2012), incorporating the restoration of stratigraphic and structural framework and the input of parameters, such as source rock geochemistry, reservoir physical properties, faults activities, basin boundary conditions, etc.

3.3.1. Structural Restoration

A two-dimensional (2D) cross-section AA′ (Figure 1B,C), through Dibei Gas Field from north to south, was selected to provide the basin framework for reconstructing hydrocarbon generation and accumulation processes. The structural restoration was based on the current 2D seismic line as interpreted provided by Tarim Oilfield, PetroChina. The position of five target wells (DB-5, YN-2, DB-102, YN-4, and YS-4 wells) from the Slope Belt to the Anticline Belt were shown in the present section AA′ (Figure 1C).

The balanced cross-section technique based on the law of conservation of mass was used to restore the structural configuration in geological periods [72,73]. The geometry is usually used to restore the structural framework of cross-sections, which follows strict assumptions of preservation of the area or length, minimization of deformation, and constant fault slips in space [74,75]. However, these ideal assumptions are not completely suitable in the foreland basin where fault-related folds are well-developed. Data from previous studies of geometric relationships between overlying folds and underlying faults were used in the study [76,77]. The time sections were pre-converted into the depth sections before BPSM to calibrate the deviation of the structure pattern. Five geological sections were selected from the balanced cross-sections: 23.3 Ma (the late stage of the Kumugeliemu Formation, $E_{1\text{-}2}k$), 12 Ma (the late stage of the Jidike Formation, N_1j), 5.3 Ma (the late stage of the Kangcun Formation, $N_{1\text{-}2}k$), 3 Ma (the middle stage of the Kuqa Formation, N_2k), and 0 Ma. In the modeling, the longest section length of 80.7 km was used as a benchmark and divided into 807 grids at the scale of 0.1 km per grid.

3.3.2. Input Parameters

- Lithology definition;
  The lithofacies data (Table 3) were derived from three wells supplied by Tarim Oilfield Research Institute. The present average porosities and permeabilities of the J_1a reservoirs in the three sub-structural belts, as represented by the YN-2, DB-102, and YS-4 wells, are 5.2% and 1.0 mD, 4.3% and 1.9 mD, and 9.5% and 7.4 mD, respectively. The reservoir porosity evolution curves assigned for individual structural belts (from the Slope Belt to the Anticline Belt) are based on porosity reconstruction considering the diagenetic history and stress–strain regimes among various geological periods;
- Source rock geochemistry;
  To depict the development of various types of source rocks, the J_2kz, J_1y, T_3t, and T_3h source rocks were divided into coal, carbonaceous mudstone, and dark mudstone in five geological sections, as reported by Wei et al. (2021) [55]. Previous studies commonly used fixed kinetics in PetroMod software based on kerogen types [78,79] but these cannot reflect the real hydrocarbon generation process in the study area. This is because of significant variations in the generative kinetics of source rocks with different organofacies (e.g., varying origins of organic matter, depositional environments, heterogeneity of sediments, geological background, etc.) [80,81]. Consequently, customized kinetics of generation for each individual source rock kerogen of different

lithologies are necessary to ensure an accurate hydrocarbon generation process in the study area [81–83]. Kinetic models obtained from sealed gold tube pyrolysis experiments by Liu et al. (2023) [84] in the northern Kuqa Foreland Basin were employed in the modeling. Since the TOC and HI values of source rocks will decrease in the process of thermal evolution [85,86], we used the method proposed by Lu et al. (2003) [87] to calculate the original TOC and HI in the early stage of hydrocarbon generation. The restored TOC and HI values are shown in Table 3;

- Boundary conditions;

Sediment–water–interface temperatures (SWIT) were determined using the global mean surface temperature based on Wygrala (1989) [88] contained in the PetroMod software. The location of the study area was set in Central Asia (latitude 41°) to automatically generate the SWIT map for the northern Kuqa Foreland Basin through time. The paleowater depth (PWD) was based on the estimation of sequence stratigraphic architecture and sedimentary facies characteristics in Kuqa Foreland Basin, defining the depth ranges for shore and shallow lacustrine (5–10 m), shallow to half deep lacustrine (10–20 m), and half deep to deep lacustrine (20–40 m) [89]. The PWDs in geological periods were calibrated from the previous studies by Guo et al. (2013) [89] and Liu et al. (2016) [63] and shown in Table 3. Heat flow data for each grid in different geological sections came from the previous studies [90,91], showing that the present heat flow in the northern Kuqa Foreland Basin is (42.5 ± 7.6) mW/m^2 [91,92] and decreases from north to the south [87]. The modeling was calibrated by changing the present heat flow values until a reasonable result was achieved.

Table 3. Input parameters used for the 2D basin modeling: SD = Sandstone, DM = Dark mudstone, CM = Carbonaceous mudstone, CO = Coal, Congl. = Conglomerate, Sand. = Sandstone, Lime. = Limestone, Gyp. = Gypsolyte, PWD = Palaeo-water depth.

Formation	Deposition Age		Erosion/ Hiatus		Lithology	Hydrocarbon Accumulation Element	PWD (m)	TOC (%)	HI (mg/g TOC)
	From (Ma)	To (Ma)	From (Ma)	To (Ma)					
Q	1.8	0			Conglomerate (typical)	Overburden Rock	0		
N_2k	5.3	1.8			Shale and Sand.	Overburden Rock	0		
$N_{1\text{-}2}k$	12	5.3			Shale and Sand.	Overburden Rock	10		
N_1j	23.3	12			Gyp. and Sand. and Congl.	Overburden Rock	10		
E	65	34	34	23.3	Congl. and Sand. and Lime.	Overburden Rock	5		
K_1b	125	112	112	65	Shale and Sand.	Overburden Rock	0		
K_1s	133.9	125			Shale and Sand.	Overburden Rock	5		
K_1y	145.6	133.9			Sand. (typical)	Reservoir Rock	5		
J_2kz-SD					Sand. (typical)	Reservoir Rock	2		
J_2kz-DM	178	165	165	145.6	Shale (organic rich, 3%TOC)	Source Rock/Seal Rock	2	3.00	250.00
J_2kz-CM					Shale (organic rich, 20%TOC)		2	51.00	300.00
J_2kz-CO					Coal (pure)		2	80.00	250.00
J_1y-SD					Sand. (typical)	Reservoir Rock	2		
J_1y-DM	198	178			Shale (organic rich, 3%TOC)	Source Rock/Seal Rock	2	2.00	280.00
J_1y-CM					Shale (organic rich, 20%TOC)		2	55.00	300.00
J_1y-CO					Coal (pure)		2	90.00	250.00
J_1a	208	198			Sand. (typical)	Reservoir Rock	0		
T_3t	216	208			Shale and Sand.	Source Rock	7	6.00	500.00
T_3h	235	216			Shale and Sand.	Source Rock	20	10.00	500.00
T_2k	245	235			Shale and Sand. and Congl.	Underburden Rock	5		
P	295	245			Congl. and Sand. and Lime.	Underburden Rock	10		
C	438	295			Sand. and Shale and Lime.	Underburden Rock	10		

4. Results

4.1. Petrography

Two types of oil inclusion assemblages (OIAs), with a yellow fluorescent color and a blue fluorescent color, are developed in the northern Kuqa Foreland Basin. The wavelengths of the maximum intensity (λ_{max}) of the fluorescence spectra were about 540 nm (yellow) and 530 nm (blue) (Figure 3). Oil inclusions assemblages predominantly occur in trails of detrital quartz grains (Figure 3). Based on the proportion of the two types of OIAs, the selected samples were divided into 'yellow samples' and 'blue samples' when the percentage of the yellow or blue fluorescing oil inclusions was up to 80% in the same sample (Table 1). One yellow sample and one blue sample were selected from the J_1y Formation with the GOI values (%) and the proportion of oil inclusions (Yellow:Blue) of 42.7%, 19:81, and 46.9%, 89:11, respectively. Two yellow samples and four blue samples were selected from J_1a Formation with the GOI values (%) and the proportion of oil inclusions (Yellow:Blue) of 45%, 98:2; 21.4%, 90:10, and 45.6%, 0:100; 62%, 0:100; 69.2%, 0:100; 67%, 0:100, respectively.

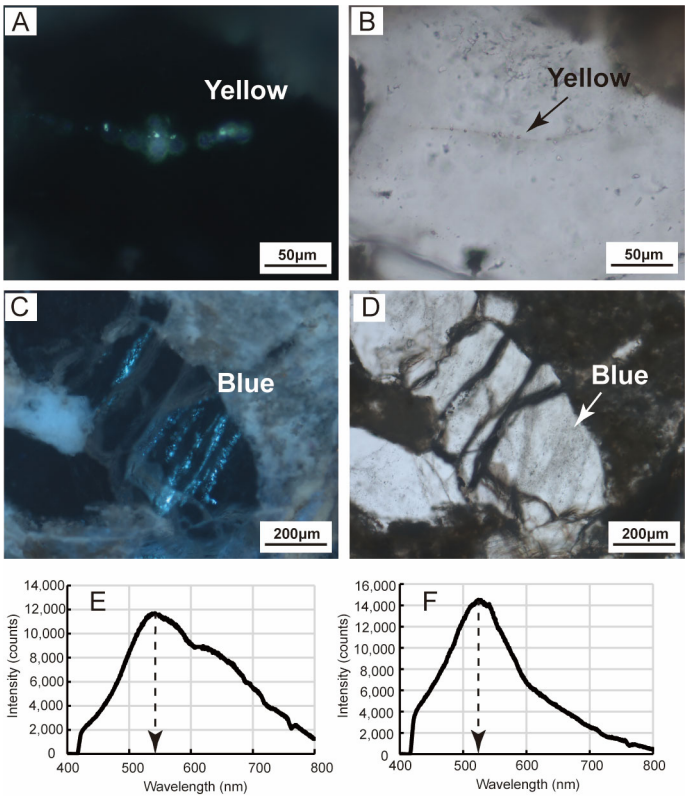

Figure 3. Photomicrographs showing two types of oil inclusions: yellow fluorescence color (**A**,**B**) and blue fluorescence color (**C**,**D**) under UV light and plane-polarized light; the fluorescence spectra of the yellow inclusions (**E**) and the blue inclusions (**F**) showing a 'blue shift' for the blue fluorescing oil inclusions (**F**) compared with the yellow fluorescing oil inclusions (**E**). Arrows indicate the wavelength of maximum fluorescence intensity.

4.2. Molecular Compositions

4.2.1. *n*-Alkanes and Isoprenoids

The gas chromatograms (GC), m/z 217 and m/z 191 mass chromatograms are shown in Figures 4–6, respectively. The source rock extracts exhibit unimodal distribution patterns of *n*-alkanes (Figure 4), with a predominance of the C_{16} and C_{14} *n*-alkanes for Jurassic source rocks (J_2kz, J_1y) and Triassic source rocks (T_3h), respectively (Table 2). In addition, the properties of the T_3t source rocks are similar to those of the J_2kz and J_1y source rocks and so are included with them in the Jurassic source rocks hereafter. The *n*-alkane distributions

show a none odd–even predominance for Jurassic source rocks and an even predominance for Triassic source rocks, and all of them display a normal distribution pattern with increasing carbon numbers (Figure 4). The ratios of isoprenoids, Pr/*n*-C_{17}, Ph/*n*-C_{18}, and Pr/Ph, are in the range of 0.3–0.79, 0.11–0.36, and 0.87–4.89, for the Jurassic source rock extracts (Table 2; Figure 7A,B), while they are in the range of 0.42–0.43, 0.21–0.25, and 0.8–0.85, for the Triassic source rock extracts (Table 2; Figure 7A,B). The Carbon Preference Index (CPI) of the Jurassic source rocks (values: 1.17–1.22) is higher than that of the Triassic source rocks (value: 1.10; Table 2).

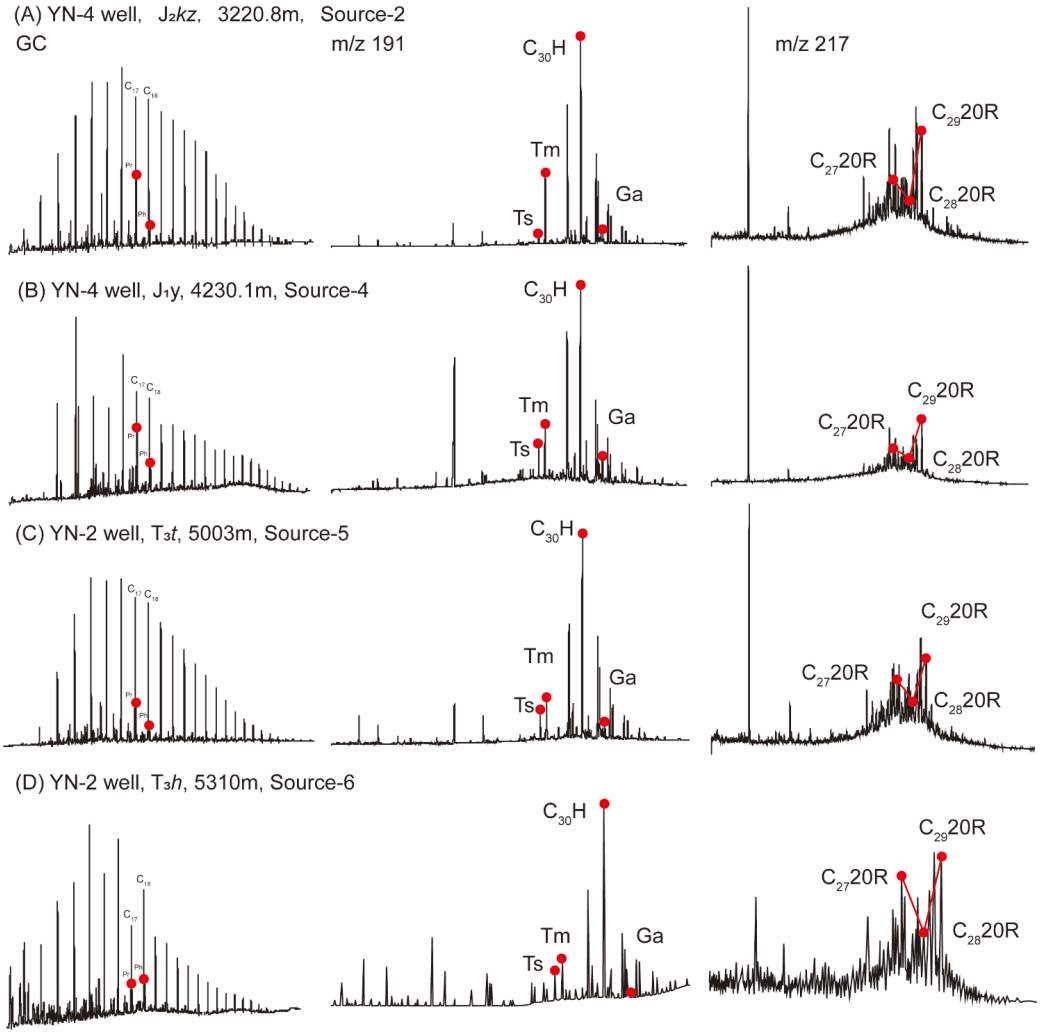

Figure 4. Total extract gas chromatograms (GC), *m*/*z* 217 and *m*/*z* 191 mass chromatograms of source rock extracts in the Dibei Gas Field. Ph = phytane; Pr = pristane; Tm = 17a(H)-trisnorhopane; Ts = 18a(H)-trisnorhopane; Ga = gammacerane; H = hopane; C_{27}20R = ααα–C_{27}(20R); C_{28}20R = ααα–C_{28}(20R); C_{29}20R = ααα–C_{29}(20R).

The distribution patterns of *n*-alkanes in the reservoir oils from the J_1y and J_1a reservoirs are very similar to those of the Jurassic source rocks (Figure 5). The reservoir oils exhibit an unimodal pattern with C_{16} *n*-alkanes as the main peaks. The ratios of Pr/*n*-C_{17}, Ph/*n*-C_{18}, and Pr/Ph for the reservoir oils from the J_1y/J_1a reservoirs are 0.21–0.24/0.1–0.23, 0.09–0.11/0.07–0.08, and 1.88–2.04/1.04–2.62, respectively (Table 2). The inclusion of oil extracts from the J_1y reservoirs is characterized by a dual peak pattern and is dominated by C_{18} and C_{28} *n*-alkanes, without odd–even predominance (Figure 5). The ratios of Pr/*n*-C_{17}, Ph/*n*-C_{18}, and Pr/Ph for the J_1y inclusion oils are in the range of 0.27–0.33, 0.12, and 0.41–0.63, respectively (Table 2). The inclusion of oil extracts from the J_1a reservoirs is

characterized by a unimodal pattern and dominated by C_{20} *n*-alkanes, without odd–even predominance or minor even predominance (Figure 5). The ratios of Pr/*n*-C_{17}, Ph/*n*-C_{18}, and Pr/Ph for the inclusion oils are in the range of 0.26–0.48, 0.2–0.59, and 0.76–1.51, respectively (Table 2).

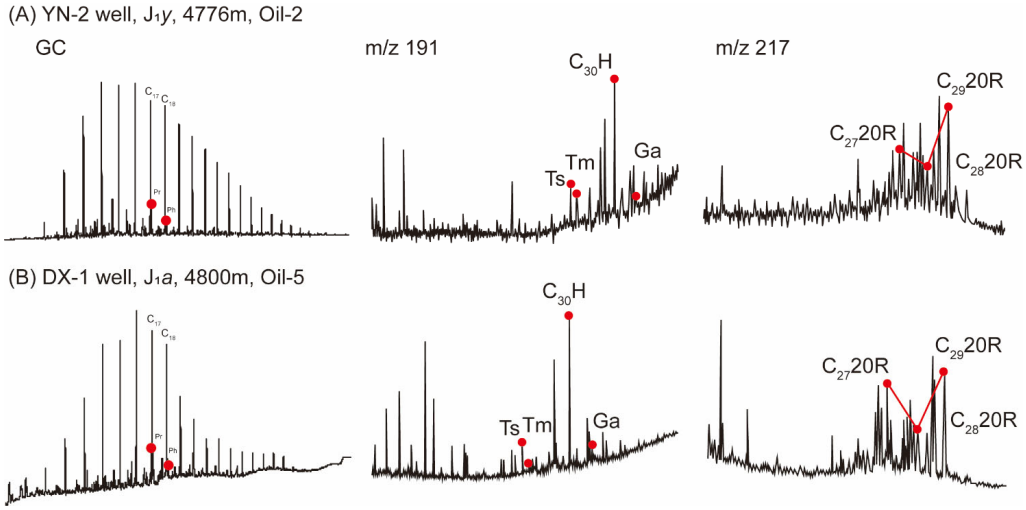

Figure 5. Gas chromatograms (GC), *m*/*z* 217 and *m*/*z* 191 mass chromatograms of the reservoir oils in the Dibei Gas Field. Peak identifications are the same as in Figure 4.

4.2.2. Steranes and Terpanes

Sterane compounds of source rock extracts show wide differences in the distributions of C_{27}–C_{29} regular steranes (Figures 4 and 7C). Extracts of the Jurassic source rocks have higher abundances of C_{29} regular steranes relative to the C_{27} regular steranes than the Triassic source rock extracts. The ratio of C_{27} regular steranes vs. C_{29} regular steranes of the Jurassic source rocks and the Triassic source rocks are in the range of 0.25–0.66 and 0.62–0.68, respectively (Table 2 and Figure 7D). Gammacerane is commonly found in these Jurassic source rocks, and the ratios of gammacerane vs. C_{30} hopane are in the range of 0.12–0.26 (Table 2 and Figure 7D). The Ts/Tm ratios and Ts/(Ts + Tm) ratios of the Jurassic source rocks are in the range of 0.22–0.93 and 0.18–0.48 (Table 2 and Figure 8A). For Triassic source rocks, the ratios of gammacerane vs. C_{30} hopane are in the range of 0.24–0.25, and Ts/Tm ratios and Ts/(Ts + Tm) ratios are in the range of 0.94–1.05 and 0.51–0.52, higher than that of the Jurassic source rocks. The isomerization ratios of C_{29} steranes ββ/(ββ + αα) and C_{29} steranes 20S/(20S + 20R) are in the range of 0.39–0.52 and 0.35–0.47 for the Jurassic source rocks and are in the range of 0.75–0.89 and 0.45–0.48 for the Triassic source rocks (Table 2 and Figure 8B).

The distributions of steranes in both the reservoir oils and inclusion oils show differential distribution patterns of diasteranes and regular steranes in the J_1y and J_1a formations (Figures 5 and 6). The ratios of C_{27} regular steranes vs. C_{29} regular steranes for most of the reservoir oils and inclusion oils show similar patterns with relatively lower values (0.38–0.7, Ave: 0.52) in the J_1y Formation compared with that in the J_1a Formation (0.79–2.09, Ave: 0.94; Table 2 and Figure 7D). A small amount of gammacerane is commonly found in all the samples with the ratios of gammacerane vs. C_{30} hopane in the range of 0.14–0.3 (Table 2; Figure 7D). For the reservoir and inclusion oils in the J_1y Formation, the Ts/Tm ratios are in the range of 0.69–1.27 and 1.04–1.21, respectively. For the reservoir and inclusion oils in the J_1a Formation, the Ts/Tm ratios are in the range of 1.57–1.73 and 1.21–1.38, higher than that of the J_1y Formation (Table 2; Figure 8A). The isomerization ratios of C_{29} steranes ββ/(ββ + αα) and C_{29} steranes 20S/(20S + 20R) are in the range of 0.51–0.67 and 0.39–0.53

for the reservoir and inclusion oils in the J_1a Formation and are in the range of 0.38–0.59 and 0.3–0.48 for the J_1y Formation (Table 2; Figure 8B).

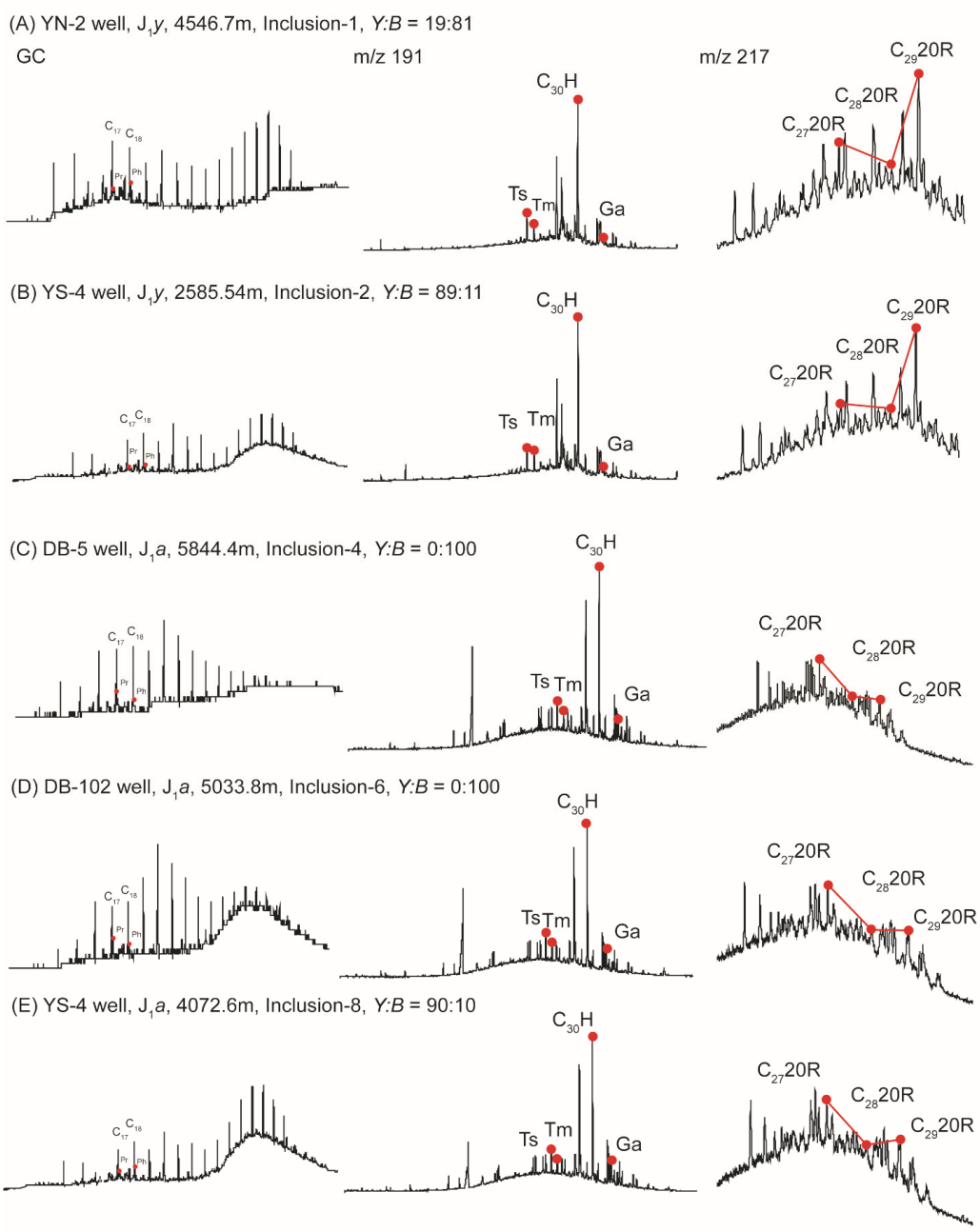

Figure 6. Gas chromatograms (GC), *m*/*z* 217 and *m*/*z* 191 mass chromatograms of the inclusion oil extracts in the Dibei Gas Field. Peak identifications are the same as in Figure 4.

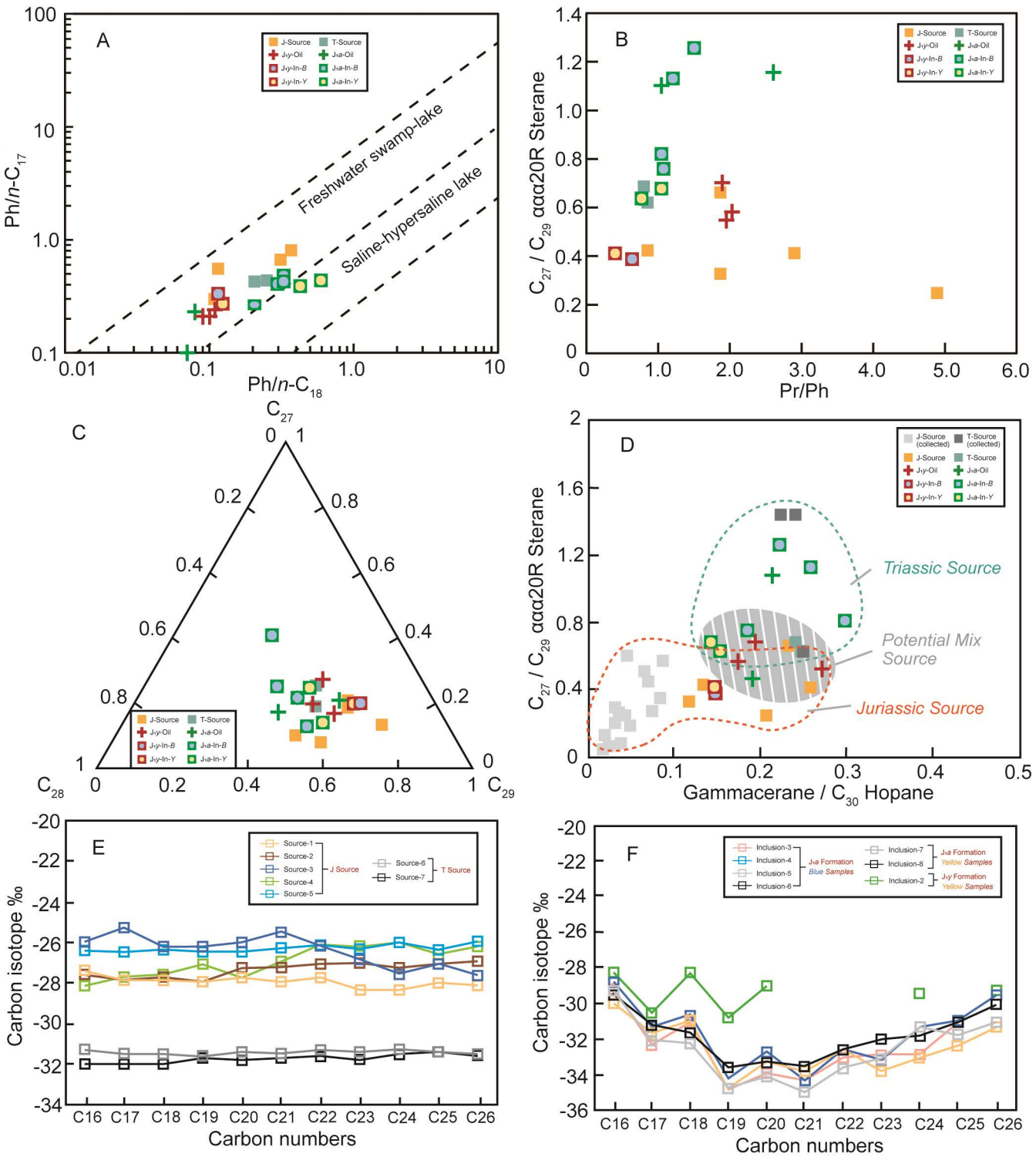

Figure 7. Cross plots of the (**A**) ternary plot of C_{27}–C_{29} regular steranes; (**B**) Pr/*n*–C_{17} vs. Ph/*n*–C_{18}; (**C**) C_{27}/C_{29} ααα20R regular steranes vs. Pr/Ph; (**D**) C_{27}/C_{29} ααα20R regular steranes vs. gammacerane/C_{30} hopane; (**E**,**F**) compound–specific carbon isotope ratios of individual *n*-alkanes of source rocks and oil inclusion extracts, respectively.

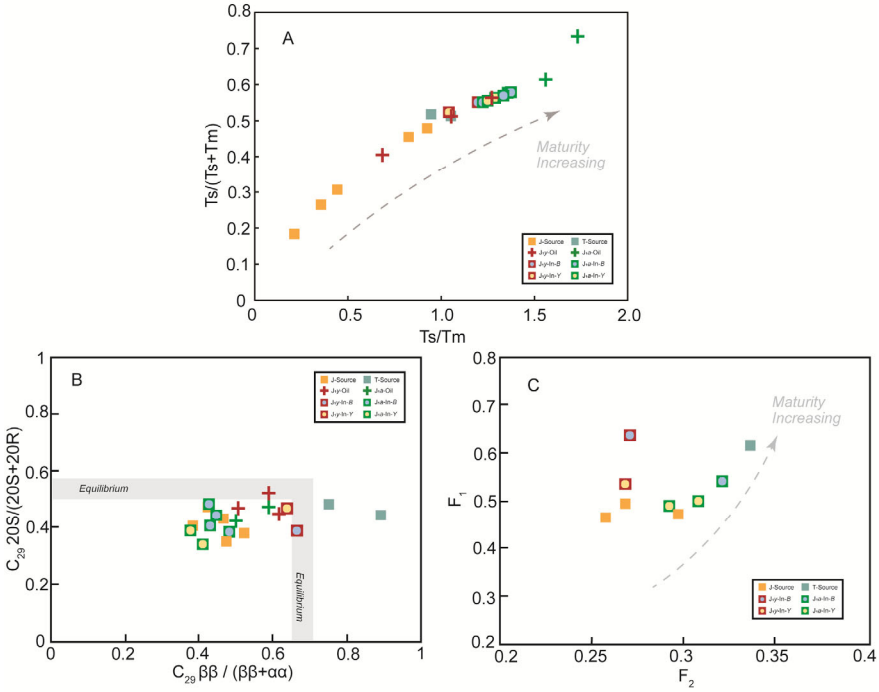

Figure 8. Cross plots of: (**A**) Ts/(Ts + Tm) vs. Ts/Tm; (**B**) C_{29} steranes 20S/(20S + 20R) vs. C_{29} steranes ββ/(ββ+ αα); (**C**) F_1 vs. F_2.

4.2.3. Aromatic Compounds

Aromatic compound parameters of the source rock extracts and inclusion oils are shown in Table 2 and Figure 8C. The methylphenanthrene ratios (F_1 and F_2) for the Triassic source rocks are systematically higher than those for the Jurassic source rocks (Figure 8C). According to the empirical relationship [93], the source rock maturity was calculated using F_1 and F_2, which range from 0.46 to 0.49 and from 0.26 to 0.30 for the Jurassic source rocks and range from 0.61 and 0.34 for the Triassic source rocks (Table 2 and Figure 8C), respectively. The F_2 values are in the average of 0.27 (n = 2) for the inclusion oils in the J_1y Formation, while they are in the range of 0.29–0.32, with an average of 0.31 (n = 3) for the inclusion oils in the J_1a Formation (Table 2 and Figure 8C). The equivalent calculated maturity levels (Rc) for the J_1y and J_1a inclusion oils have averages of 0.88% Rc and 1.00% Rc, indicating mature oils. The 'yellow samples' have a lower maturity than the 'blue samples' (Table 2 and Figure 8C).

4.2.4. Carbon Isotopic Characteristics

For source rock extracts, the carbon isotope contents (‰) of individual n-alkanes range from −28‰ to −26‰ and from −34‰ to −31‰ in the Jurassic and Triassic source rocks, respectively (Figure 7E). For the inclusion oils, the carbon isotope contents (‰) of individual n-alkanes range from −31‰ to −28‰ and from −35‰ to −30‰ in the J_1y and J_1a Formation, respectively (Figure 7F).

The carbon isotope ratios of the light gases from the Jurassic reservoirs are shown in Figure 9. The $\delta^{13}C_1$ values of the samples are in the range of −37‰ to −30‰, while the $\delta^{13}C_2$ values of the samples are in the range of −28‰ to −23‰, and the $\delta^{13}C_3$ values of the samples are in the range of −27‰ to −22‰.

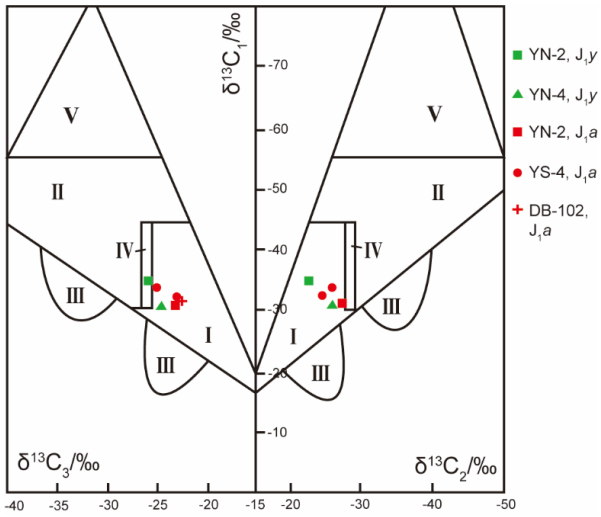

Figure 9. Carbon isotope ratios of natural gas components, showing the main coal measure sources with a minor lacustrine input. I: humic gas; II: sapropelic gas; III: isotopic inversion region due to mixed origin; IV: mixed humic gas and sapropelic gas; V: biogas and sub–biogas.

4.3. Multivariate Statistical Results

4.3.1. HCA Results

Based on HCA analysis of the 11 geochemical parameters (Table 2), two types of source rocks have been identified (Figure 10): the Jurassic source rocks and the Triassic source rocks. The majority of reservoir oils and inclusion oils from the J_1a Formation belong to an oil family generated from the Triassic source rocks. The inclusion oils from the J_1y Formation are related to the Triassic sources, while the reservoir oils from the J_1y Formation and the outlier reservoir oil from the J_1a Formation are genetically related to the Jurassic sources (Figure 10).

4.3.2. PCA Results

The 11 geochemical parameters used for principal component analysis (PCA) are the same as those used for the HCA and are shown in Table 2. The results show that the cumulative variance contribution of the top five principal components (PCs) accounts for nearly 90% of the data. Consequently, PC1 to PC5 was selected to distinguish the geochemical relationship among the oil samples. The PCA loadings and score data used for oil–source correlation are shown in Tables 4 and 5, and Figure 11.

Table 4. The loadings data for the parameters for PCA. R1 to R12 are shown in Table 2.

Biomarker Ratios	Principle Components (PC)				
	PC1	PC2	PC3	PC4	PC5
R1	0.815	0.256	−0.306	−0.123	−0.130
R3	−0.875	−0.146	0.116	0.072	0.019
R4	−0.398	−0.242	−0.147	0.820	−0.012
R5	−0.052	−0.204	−0.028	−0.078	0.957
R6	−0.162	−0.661	−0.232	0.638	−0.083
R7	0.108	−0.379	−0.637	0.409	−0.342
R8	0.492	0.805	−0.099	−0.131	−0.054
R9	0.076	0.890	0.143	−0.116	−0.357
R10	0.814	0.027	0.420	−0.217	0.037
R11	−0.043	0.087	0.908	−0.034	−0.231
R12	−0.050	−0.145	0.667	−0.526	0.341

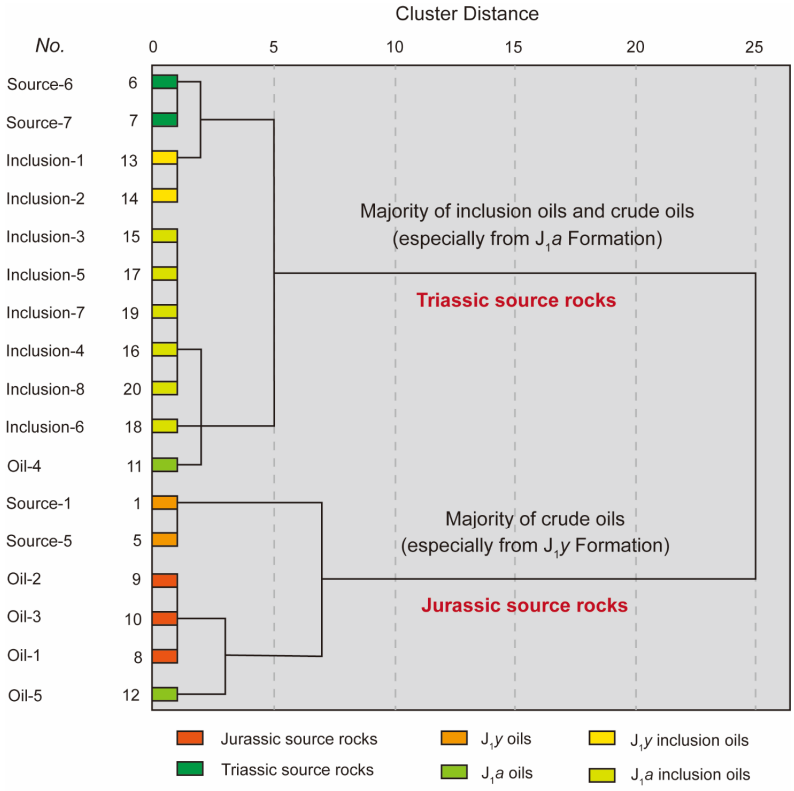

Figure 10. Hierarchical cluster analysis (HCA) results identify two oil families, with oils from the J_1a formation mainly derived from the Triassic source rocks, while those from the J_1y Formation mainly derived from the Jurassic source rocks. Sample numbers and selected parameters are shown in Tables 1 and 3, respectively.

Table 5. The score data of the samples for PCA.

Samples	Wells	Formations	No.	PC1	PC2	PC3	PC4	PC5
Source-1	YN-2	J_2kz	1	−1.522	−1.525	−0.153	1.043	0.772
Source-3	YN-2	J_2kz	3	−0.786	−1.827	−0.777	0.573	0.508
Source-6	YN-2	J_1y	6	0.570	−0.978	1.362	−0.244	−1.106
Source-7	YN-2	J_1y	7	0.682	−0.720	1.998	0.723	−1.098
Oil-1	YN-2	T_3t	8	−0.494	−0.710	−0.086	−1.414	1.031
Oil-2	YN-2	T_3h	9	0.213	0.099	0.974	−0.773	1.072
Oil-3	YN-2	T_3h	10	0.049	−0.127	0.126	−1.168	0.565
Oil-4	DB-104	J_1y	11	0.766	1.498	−0.520	−1.161	−0.089
Oil-5	DX-1	J_1y	12	−0.486	1.446	0.527	0.298	2.298
Inclusion-1	YN-2	J_1y	13	−1.507	1.294	0.504	0.081	−1.082
Inclusion-2	YS-4	J_1a	14	−1.534	1.123	0.959	0.401	−1.010
Inclusion-3	DB-5	J_1a	15	0.349	0.702	−0.942	1.686	−0.098
Inclusion-4	DB-5	J_1y-B	16	1.078	−0.655	−0.007	−1.516	−0.396
Inclusion-5	DB-102	J_1y-Y	17	1.745	0.233	−0.405	1.473	0.175
Inclusion-6	DB-102	J_1a-B	18	1.423	0.171	−0.168	0.823	0.529
Inclusion−7	YN−2	J_1a-B	19	−0.148	−0.180	−1.710	−0.183	−0.835
Inclusion−8	YS−4	J_1a-B	20	−0.400	0.156	−1.682	−0.644	−1.236

The coefficient in the loadings plot shows either a positive or negative correlation between the variables and PCs, and the greater the absolute value is, the stronger the correlation would be (Table 4). For example, PC1 is mainly influenced by two source variables, $C_{27}/(C_{27} + C_{28} + C_{29})$ regular steranes (R1) and gammacerane/C_{30} hopane (R10), with positive correlation coefficients of 0.815 and 0.814 (Table 4), respectively, showing a strong linkage to the sedimentary environment. The scores plot of PC1 to PC5 show that the source rock samples can be clearly separated into two distinct genetic families (Figure 11A), with higher score values in PC4 and PC5 for the Jurassic source rocks while

there are higher score values in PC1, PC3, and PC4 for the Triassic source rocks. The reservoir oils from the J_1y Formation have higher score values in PC3 and PC5, whereas the reservoir oils from J_1a Formation have higher score values in PC2 and PC5 (Figure 11B). For the inclusion oils, samples from the J_1y Formation have higher score values in PC2, PC3, and PC4 (Figure 11C), while the samples from the J_1a Formation have higher score values in PC1 and PC4 (Figure 11D). The cross plot of PC1 vs. PC5 shows distinct correlations between the Jurassic source rocks and the J_1y oils, the Triassic source rocks and the J_1a oils; however, some crude oils from the J_1a formation also appear to correlate with the Jurassic source rocks (Figure 11E).

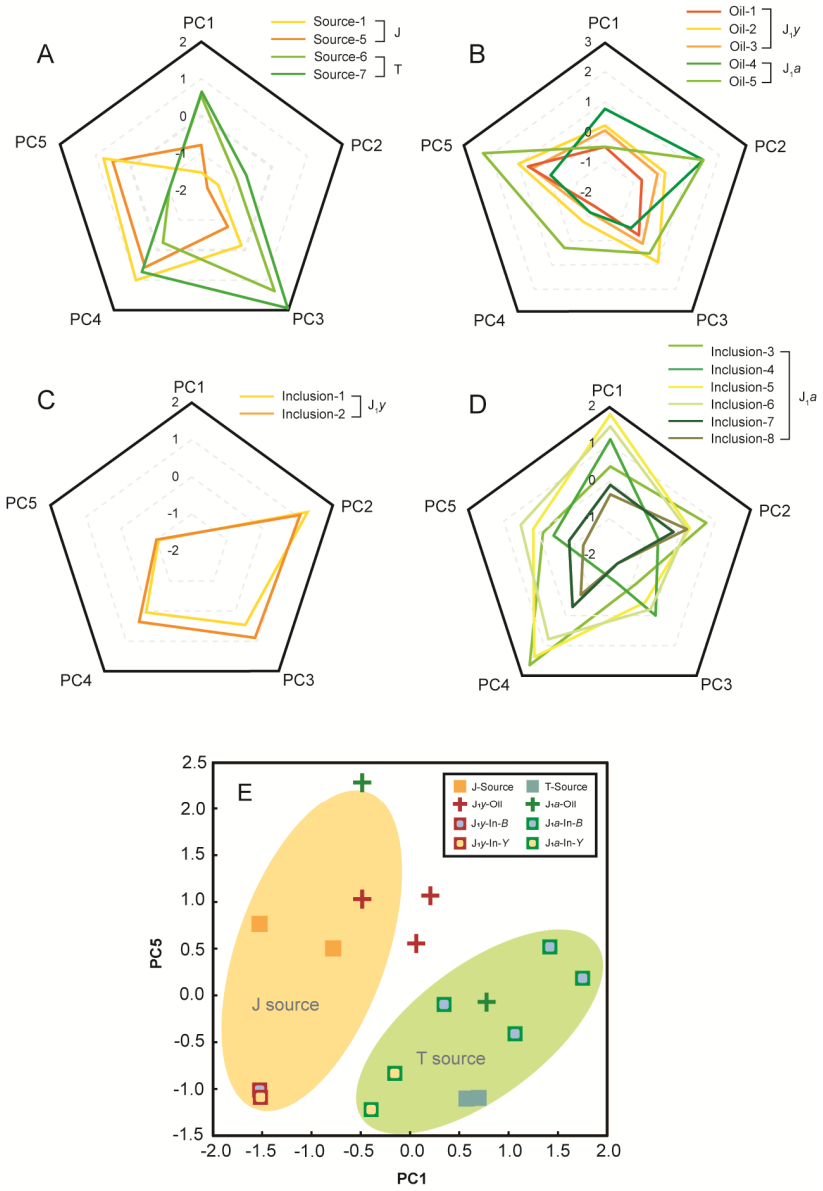

Figure 11. PCA score plot of the five principal components from the source rock extracts (**A**,**B**), reservoir oil extracts (**C**), inclusion oil extracts (**D**), and the cross plot of PC1 and PC5 (**E**), reflecting the similarity between the Jurassic source rocks and the J_1y oils, Triassic source rocks, and the J_1a oils. Mix sources are seen among all the oils. See Table 1 for sample information.

4.4. Basin Modeling Results

4.4.1. Hydrocarbon Generation and Accumulation History

Vitrinite reflectance (Ro) serves as a measure of the maturity of the source rocks. The Easy% Ro Model is the most widely used model in the study of paleo-temperature. In this

study, the thermal histories of the source rocks from section AA′ were modeled based on the Easy% Ro routine, which is applicable in the range of 0.3–4.5%. The modeling results have a good fit to the measured Ro values (Figure 12).

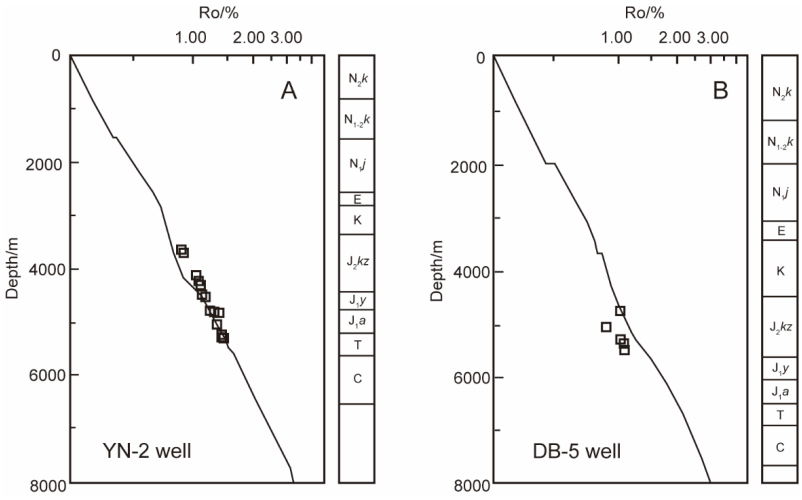

Figure 12. Calibration of the thermal history model, showing that the measured Ro and calculated Ro values in YN–2 well (**A**) and DB–5 well (**B**) from the AA′ section across the Dibei Gas Field are in good agreement.

Figures 13 and 14 show the results of the hydrocarbon generation, migration, and accumulation modeling of the cross-section AA′ at spatial and temporal scales. The results are shown as follows. (1) At 23.3 Ma, both the Triassic source rocks and Jurassic source rocks were low-mature with Ro values of 0.55–0.8% and generated a small amount of early oil (Figures 13A and 14A). (2) At 12 Ma, the uplift of the southern Tianshan Mountains resulted in the differential burial of strata from north to south, with the result that the source rocks in the Sag Belt matured rapidly at this stage (Figure 13B). The Triassic source rocks and a minor amount of the Jurassic source rocks in the Sag Belt became highly mature, with the generation of a quantity of wet gas (1.3–2.0% Ro), while most of the Jurassic source rocks in the Sag Belt became mature, with the generation of a large amount of late oil (1.0–1.3% Ro) (Figures 13B and 14B). At this time, most of the source rocks in the Slope Belt entered the oil generation stage, with the mature oil (0.7–1.0% Ro) generated from the Triassic source rocks and the low-mature oil (0.55–0.7% Ro) generated from the Jurassic source rocks. (3) At 5.3 Ma, the source rocks in the Slope Belt entered the main oil generation stage (0.7–1.3% Ro), and most of the source rocks of the Sag Belt entered the wet gas generation stage (1.3–2.0% Ro, Figure 13C). Large amounts of light oil and gas migrated into the Jurassic reservoirs via unconformities and faults, forming significant accumulations in the zones of trap development (Figure 14C). (4) At 3 Ma, with the deposition of the extremely thick Kuqa Formation (N_2k), the strata were buried rapidly to depths ranging from 4000 m to 8000 m. The source rocks reached the dry gas, wet gas, and late oil generation stage in the Sag Belt through to the Slope Belt, respectively (Figure 13D). Gas generated from the Sag Belt and Slope Belt and the oil generated from the Slope Belt and Anticline Belt co-charged the Jurassic reservoirs (Figure 14D). (5) At present, the transformation ratio (TR) of the Jurassic source rocks reaches 70% in the Sag Belt, 20% to 40% in the Slope Belt, and only 10% in the Anticline Belt (Figure 15). For the Triassic source rocks, the TR values reach 90% near or in the Sag Belt, 30% to 60% in the Slope Belt, and 20% in the Anticline Belt (Figure 15).

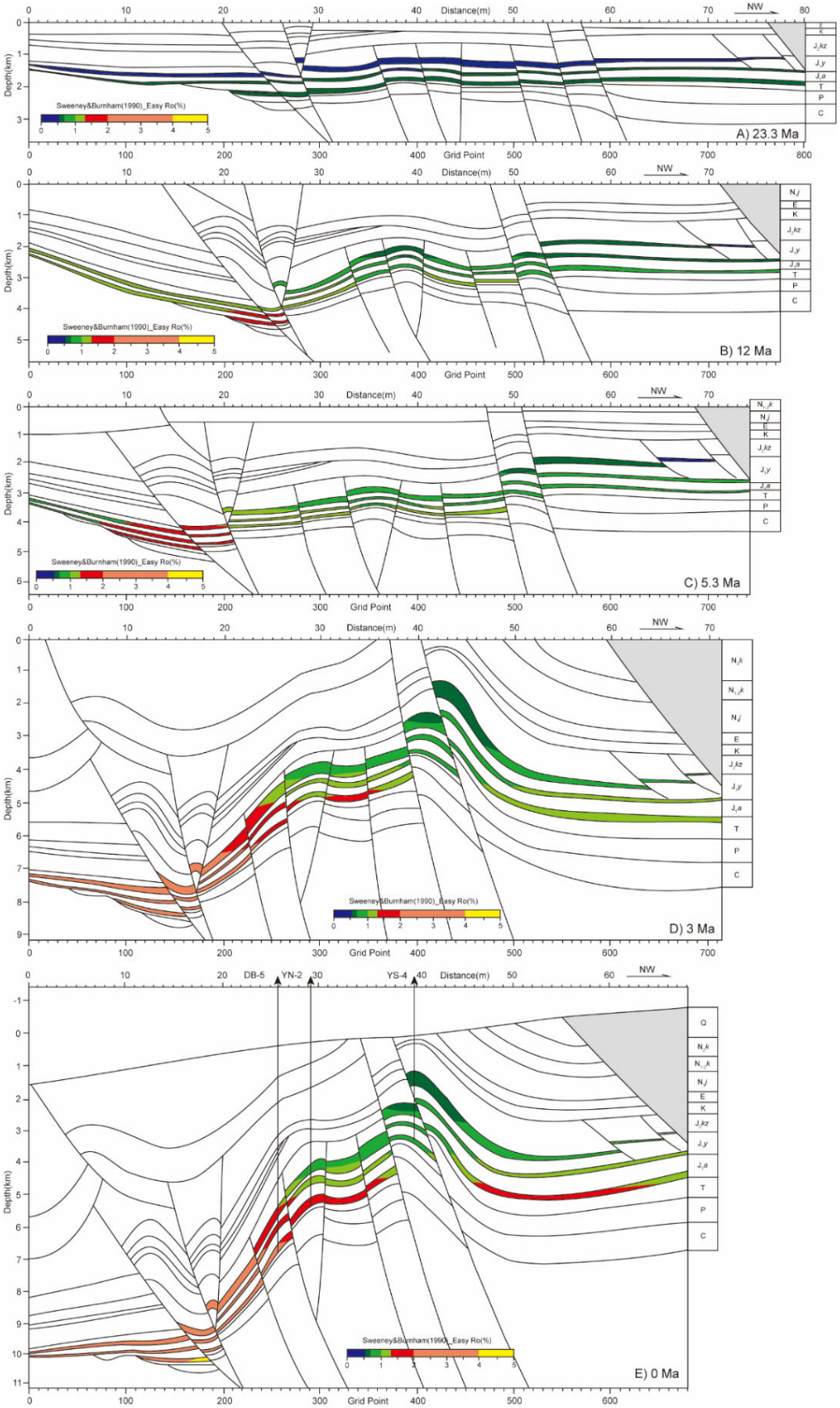

Figure 13. Thermal maturity evolution of the J_2kz, J_1y, T_3t, and T_3h source rocks in the AA′ section at five geological periods in the northern Kuqa Foreland Basin. (**A**) 23.3 Ma; (**B**) 12 Ma; (**C**) 5.3 Ma; (**D**) 3 Ma; (**E**) Present.

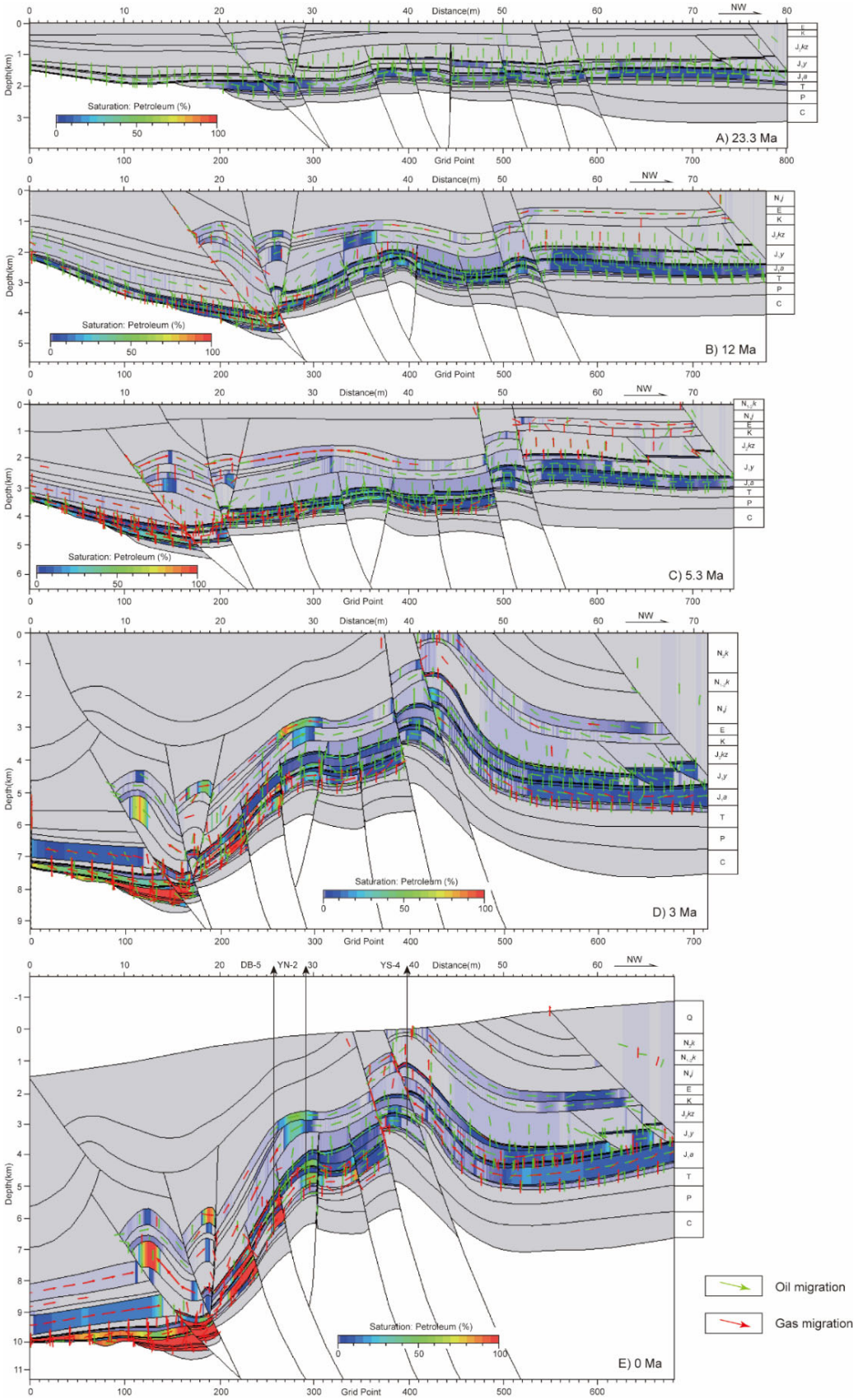

Figure 14. Hydrocarbon migration pathways and hydrocarbon saturation in the AA′ section at five geological periods in the northern Kuqa Foreland Basin. (**A**) 23.3 Ma; (**B**) 12 Ma; (**C**) 5.3 Ma; (**D**) 3 Ma; (**E**) Present.

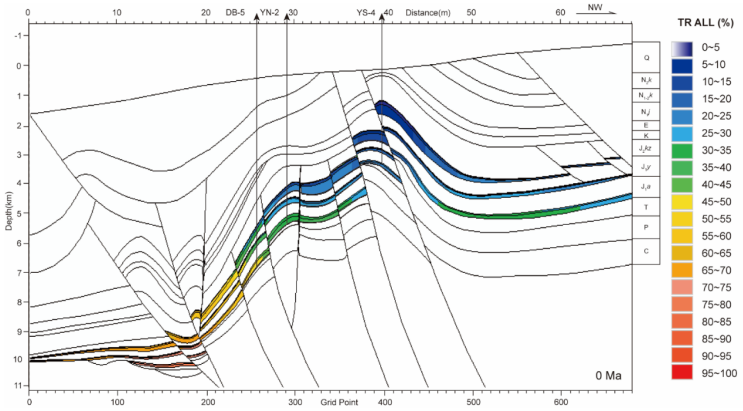

Figure 15. Transformation ratios (TR) of the source rocks in the AA′ section at present in the northern Kuqa Foreland Basin, showing a decreasing trend from the Sag Belt to the Central Anticline Belt.

4.4.2. Mass of Hydrocarbon Generation

The mass of hydrocarbon generation from the two types of source rocks (J_2kz, J_1y, T_3t, and T_3h) were calculated and compared. The results indicate the following. (1) The main stage of oil generation occurred in the interval from 23.3 Ma to 12 Ma, and the main gas generation occurred from 5.3 Ma to 3 Ma, accompanied by a small amount of gas formed by oil cracking (Figure 16A). (2) The Sag Belt was the main area of oil generation in the early stage of 145.6 Ma–12 Ma, while the contribution of source rocks in the Slope Belt and Anticlinal Belt increased during the late stage of 12.5 Ma–0 Ma (Figure 16B). The gas was generated mainly in the Sag Belt, with increasing contributions from the Slope and Anticline in the late stage (Figure 16B). (3) In the early stage, the T_3h lacustrine source rocks were the principal source of oil generation, while oil generation mainly occurred in the J_2kz, J_1y, and T_3t coal measure source rocks after 23.3 Ma (Figure 16C). The amounts of gas generated from the coal measure source rocks have increased greatly from 5.3 Ma to the present (Figure 16C). (4) The amount of oil and gas from dark mudstones was predominantly in the study area. The occurrences of petroleum in the basin are the result of generation from a combination of different source rocks since 23.3 Ma (Figure 16D).

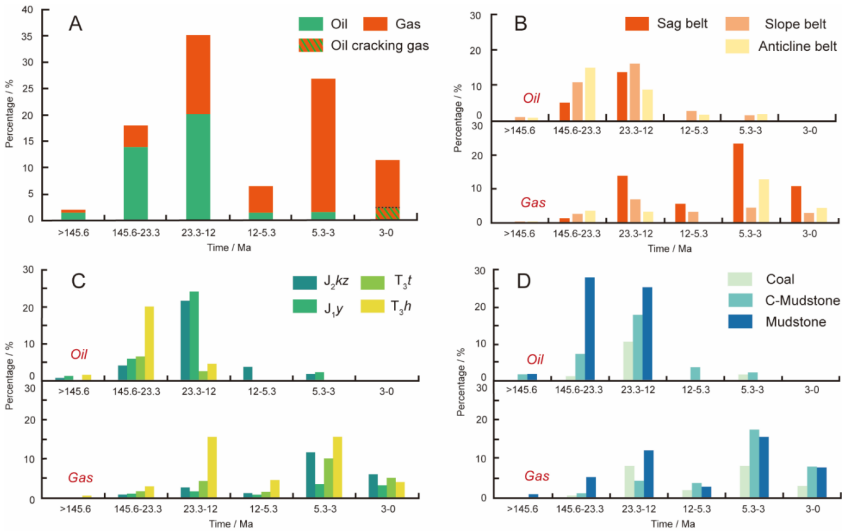

Figure 16. Hydrocarbon generation of two types of source rocks at different geological times in the northern Kuqa Foreland Basin, showing the evolution of oil and gas generation (**A**); hydrocarbon generation among different sub-structural belts (**B**); hydrocarbon generation from different types of source rocks (**C**); hydrocarbon generation from different lithologies (**D**). The histogram is formed by the calculated percentages of the total hydrocarbon generation in all geological time.

5. Discussion

5.1. Source Rock Characteristics

Two types of source rocks have been identified in the northern Kuqa Foreland Basin, consistent with the previous studies of Li et al. (2019) [4] and Tang et al. (2021) [5]. One source is Jurassic coaly source rocks, and the second is Triassic lacustrine source rocks. According to the source rocks evaluation in previous studies (Table 6), the Triassic source rocks (T_3h) are predominantly by Type II_2 and III organic matters, and the average TOC value is 1.84 wt%, the average $S_1 + S_2$ value is 14.07 mgHC/g rock, HI values are in the range of 16 mgHC/gTOC–189 mgHC/gTOC, and T_{max} values are in the range 439–469 °C. The Jurassic source rocks (J_2kz, J_1y, and T_3t) are predominantly Type III with minor Type II organic matters, and the average TOC is 18.32 wt%, the average $S_1 + S_2$ value is 27.61 mg HC/g rock, HI values are in the range of 12 mgHC/gTOC–901 mgHC/gTOC, and T_{max} values are in the range of 405–546 °C. Both types of source rocks display predominantly good to excellent petroleum-generation qualities.

Table 6. Total organic carbon parameters of the source rocks in the northern structural belt (modified from Li et al., 2019 [44] and Gao et al., 2022 [94]).

Formation	Lithology	Type of Organic Matter	TOC (Average)	$S_1 + S_2$ (Average)	HI (Average)	T_{max}
J_2kz	DM	III and II_2	0.01~2.96 (1.08)	0.04~6.92 (1.56)	11.68~79.00 (55.55)	430~546
J_2kz	CM	III	0.62~33.1 (16.94)	14.91~76.38 (45.60)	52.00~54.00 (166.83)	431~446
J_2kz	CO	III	42.62~53.75 (45.57)	43.78~71.37 (56.73)	83.17~161.07 (118.53)	425~432
J_1y	DM	III and II_2	0.01~15.30 (2.82)	0.11~42.03 (9.68)	19.00~901.00 (144.64)	405~503
J_1y	CM	III	11.13~36.86 (21.83)	10.04~94.11 (33.10)	79.00~302.00 (140.44)	428~443
J_1y	CO	III	21.65~68.23 (37.91)	17.18~95.49 (43.27)	70.00~245.00 (141.99)	435~462
T_3t	CM	III	1.62~2.96 (2.08)	1.43~10.88 (3.30)	46.00~278.00 (102.86)	429~445
T_3h	CM	II_2 and III	0.26~7.29 (1.84)	0.11~88.84 (14.07)	16.00~189.63 (80.79)	439~469

Note: DM = Dark mudstone, CM = Carbonaceous mudstone, CO = Coal, TOC = total organic carbon (wt.%), S_1 = soluble hydrocarbon content; S_2 = pyrolysis hydrocarbon content; HI = hydrogen index, T_{max} = pyrolysis temperature corresponding to the highest point of P_2 peak (°C).

The Pr/Ph ratios for the Triassic source rocks are generally less than 1 (Table 2), indicating that nearly all of the source rocks were deposited under anoxic conditions [17,95,96]. The Pr/Ph ratios for the Jurassic source rocks are greater than one (Table 2), indicating that the sedimentary environment of the source rocks changed from the reduced deep lacustrine facies to the shallow marsh and near-shore-shallow lacustrine facies [17,97,98]. The cross plots of Pr/n-C_{17} vs. Ph/n-C_{18} and C_{27}/C_{29} regular steranes vs. Pr/Ph show that the source rocks are mainly generated from freshwater swamp-saline lake environments. The Triassic sources appear to have been influenced more by saline-hypersaline lake compared with the Jurassic source rocks (Figure 7B,C). The relative abundances of C_{27}–C_{28}–C_{29} regular steranes are a common parameter indicative of the input of organic matter [23,99,100]. Higher levels of C_{29} steranes occur in higher plants, showing an inverted "L" shape of C_{27}–C_{28}–C_{29} regular steranes distribution in the Jurassic source rocks (Figure 4A–C). Higher relative levels of C_{27} sterane (or C_{28} sterane) occur in the aquatic inputs, showing a "V" shape of C_{27}–C_{28}–C_{29} regular steranes distribution in the Triassic source rocks (Figure 4D) [99]. Gammacerane is a pentacyclic triterpane that originated from tetrahymanol, and the latter is formed by a protist or other bacterium that replaces lipid compounds [17,101]. The gammacerane/C_{30} hopane ratio is greater than 0.11 in all the source rock extracts (0.12–0.26), indicating the potential water column stratification [102]. The occurrences of gammacerane may also be influenced by hypersaline depositional environments [17,103]. In summary, the Triassic source rocks are predominately composed of lacustrine source rocks, and the Jurassic source rocks are predominately composed of coaly source rocks.

The results of gas chromatograms (GCs) are characterized by a none odd–even predominance of the Jurassic source rocks (CPI: 1.17–1.22) and an even predominance of the Triassic source rocks (CPI: 1.10; Figure 4 and Table 2), reflecting a higher thermal maturity of the Triassic source rocks compared with that of the Jurassic source rocks [10,19]. The isomerization ratios of C_{29} steranes $\beta\beta/(\beta\beta + \alpha\alpha)$ and C_{29} steranes 20S/(20S + 20R) are common thermal maturity characterization parameters with an equilibrium value being at 0.9% Ro [17,104]. The results show higher maturity of Triassic source rocks than that of Jurassic source rocks, with some of them exceeding the end point of isomerization (Figure 8B). Methylphenanthrene with the methyl group at the α– position will be transformed into a more stable one at the β– position with increasing maturity. Radke et al. (1982) [105] proposed methyl phenanthrene indexes (MPI-1, MPI-2) to measure the maturity of organic matter. These ratios are sensitive to thermal evolution but may become inefficient for high-maturity oils. Methyl phenanthrene ratios (F_1, F_2) with greater applicability at higher levels of maturity. The F_1 and F_2 values of the Jurassic source rocks and Triassic source rocks are, on average, 0.48 and 0.27 and 0.61 and 0.34, respectively (Table 2 and Figure 8C). The calculated maturities from F_1 and F_2 values of the two types of sources are the average of 0.96% Rc and 0.89% Rc and 1.32% Rc and 1.1% Rc (Table 2), respectively, indicating the higher maturity of Triassic source rocks than the Jurassic source rocks. The calculated % Rc is the same as the measured Ro (Figure 12) and the basin modeling results (Figure 13).

5.2. Oil–Source Correlation

5.2.1. Different Oil–Source Correlations

The *m*/*z* 217 mass chromatograms in both the reservoir oils and inclusion oils of J_1y Formation show an inverted "L" distribution, which is similar to the Jurassic coaly source rocks (Figures 5 and 6). The key biomarker parameters show that the reservoir oils and inclusion oils from the J_1y Formation have a close similarity to the Jurassic coaly source rocks, but there are also some similarities to the Triassic sources. For example, the C_{27}/C_{29} regular sterane vs. gammacerane/C_{30} hopane plot shows that the J_1y reservoir oils or inclusion oils trend somewhat in the direction of the Triassic sources (Figure 7D). The trend of the carbon isotopic ratios of the individual *n*-alkanes of the J_1y oil inclusion extract is located between the Jurassic and Triassic source rocks (Figure 7F). In the HCA results, the inclusion oils of J_1y are classified as a Triassic-sourced fluid, while the reservoir oils of J_1y are classified as a Jurassic-sourced fluid (Figure 10). The mixed sources are shown in the score plots of PCA, which also confirms that the reservoir oils contain more coaly sources inputs than the inclusion oils (Figure 11E).

The reservoir oils and inclusion oils of J_1a Formation show a similar "V" distribution in *m*/*z* 217 mass chromatograms with the Triassic lacustrine source rocks (Figures 5 and 6). The C_{27}/C_{29} regular sterane vs. gammacerane/C_{30} hopane plot also shows that the J_1a reservoir oils and inclusion oils have a distinct similarity to the Triassic sources, except for one reservoir oil sample with a slight shift toward the Jurassic sources (Figure 7D). The carbon isotopic compositions of the individual *n*-alkanes of the J_1a oil inclusions are close to the Triassic sources (Figure 7F). In the HCA and PCA results, the majority of inclusion oils and reservoir oils of J_1a are classified as being from a Triassic source, and only a few reservoir oil samples may have Jurassic origins (Figures 10 and 11).

The analysis of oil inclusions shows that the maturity of 'blue samples' is higher than that of 'yellow samples' in the same layer (Table 2, Figures 3 and 8). However, samples from the same layer with two types of oil inclusions show no significant differences in the source (Figures 7F, 10 and 11E). Consequently, the differences in fluorescence colors are mainly the result of variations in oil charge timing, reflecting the maturity of the oils, and

not due to differences in the source types of the fluid. That is, the inclusion oils from the same interval have the same source organic matter type.

5.2.2. Potential Oil–Source Changing

Individual traps containing fluids from multiple sources are a difficult problem in oil–source correlation analysis [14]. Multivariate statistical analysis is widely used to reduce the complexity associated with variations in the deposition and maturity of samples and the degree of oil mixing in oil–source correlation [4,5]. The differences in geochemical characteristics between reservoir oils (present) and inclusion oils (paleo) show a possible change in source types over geologic time. This possibility is supported by the HCA, PCA, and basin modeling results, which demonstrate a trend of increasing hydrocarbon generation in the Jurassic coaly sources through time (Figures 10, 11 and 16). In HCA and PCA analysis, the reservoir oils exhibit a higher input of higher terrestrial plants than the inclusion oils (Figures 10 and 11). The differences between the reservoir oils and inclusion oils are probably influenced by the rapid maturation of Jurassic source rocks during the late Himalayan orogeny (Figure 13). Significant amounts of hydrocarbons have been generated in the Jurassic coal measures since ~5 Ma (Figures 13 and 16C). The levels of maturity and transformation ratios (TR) indicate that Jurassic coaly source rocks can have significant source rock potential in the area, especially the shallow buried source rocks located in the Slope Belt and Anticline Belt (Figure 15).

5.3. Gas Sources

There are still uncertainties about the origins of the gas in the Kuqa Foreland Basin. It has been proposed that the gas condensate is gas cracked from oil or from kerogen due to the heating of Paleozoic source rocks in Kela 2 Gas Field and Kokyar Gas Field [106,107]. However, further investigations have demonstrated that the Middle and Lower Jurassic coal measures are the main sources of the gas condensate in Dabei Gas Field, Di'na2 Gas Field, and Dibei Gas Field [48,108,109]. It has also been suggested that the gas comes from a mixing of coal-derived gas with petroliferous gas [48,110]. The modeling results show that gas from oil cracking is not the main source of the gas (Figure 16A). The condensate gas accumulated in the Dibei Gas Field is dominated by humic gas, with minor mixing of sapropelic gas (Figure 9), and derived mainly from the Jurassic coaly source rocks.

5.4. Hydrocarbon Accumulation History

At *c.a.* 23.3 Ma, a minor amount of low-maturity oil from the Anticline Belt migrated to the Jurassic reservoirs (Figures 14A and 16) to form the early oil inclusions in the paleo-structures. These are the yellow-fluorescing oil inclusions, with low maturity (Ave: ~0.8% Rc) in the Anticline Belt (Table 2, Figures 3 and 8). At this stage, the oils were generated mainly in the Triassic lacustrine dark mudstones (Figure 16).

Between 23 Ma and 12 Ma, the tectonism of the late Himalayan orogeny resulted in the hydrocarbon generation zones gradually expanding from the Sag Belt to the Slope Belt (Figure 14B,C). Wet gas accompanied by light oil from the Triassic source rocks in the Sag Belt migrated and charged the Jurassic reservoirs via Triassic unconformities and secondary thrust faults (Figure 16). These hydrocarbons formed large numbers of blue fluorescing oil inclusions with relatively high maturity (Ave: ~1.0% Rc) (Table 2 and Figure 3). Subsequently, the Jurassic source rocks entered the main oil-generating stage (Figure 16), and the oil inclusions occurring in the J_1y reservoirs contain oils of Jurassic origin mixed with the Triassic source oils (Figure 5A,B).

From 5 Ma to the present, nearly all of the source rocks entered the gas generation stage, with the expulsion of large quantities of wet gas and dry gas, except for some zones in the Slope Belt and Anticline Belt that are still in the oil generation window (Figure 13,

Figure 14D,E and Figure 16). The reactivation of secondary thrust faults provided the pathways for large-scale gas migration and accumulation in the traps developed in the Slope Belt [43,44,58] when the Anticline core was breached by the Yiqikelike deep-root fault at this stage [42]. The Jurassic source rocks then became the most important sources for late-stage hydrocarbon generation (Figure 16), and consequently, reservoir oils and condensate gas in the J_1y and J_1a reservoirs have a significant input from the Jurassic sources (Figures 9–11). This indicates a high potential for the occurrence of petroleum generated from the Jurassic source rocks elsewhere in the Kuqa Foreland Basin, particularly in the Slope Belt, where the transformation ratio of these sources is 30% to 60%.

6. Conclusions

Based on the molecular geochemical correlations of source rocks, reservoir and inclusion oils, multivariate statistical analysis (HCA, PCA), and basin modeling, the sources of hydrocarbon in the northern Kuqa Foreland Basin can be summarized as follows.

(1) A Jurassic coaly source rock and a Triassic lacustrine source rock are identified in the northern Kuqa Foreland Basin, with their relative contribution to the Dibei Gas Field evolving over time;

(2) Geochemistry, multivariate analysis, and basin modeling results for both reservoir oils and inclusion oils indicate multiple sources of oils in the Dibei area. The early-charged oils recorded by oil inclusions were mainly generated from the Triassic lacustrine source rocks, with slight differences between J_1y and J_1a formations. The inclusion oils in the J_1y reservoirs were generated mainly by the Triassic lacustrine source rocks but with minor Jurassic coaly input; whereas, the inclusion oils of the J_1a reservoirs were generated mainly from the Triassic lacustrine source rocks. In contrast, the present reservoir oils show a significant input from the Jurassic sources. The difference between reservoir oils and inclusion oils shows a switching in oil–sources;

(3) At ~23.3 Ma, the low-mature oils were mainly originated from the Triassic source rocks. From 23.3 Ma to 12 Ma, oil–sources gradually changed from the Triassic source rocks to the Jurassic source rocks due to a rapid burial, which caused all the source rocks to reach the oil generation window. At ~5 Ma, most oil and gas were generated mainly from the Jurassic source rocks. The Jurassic coaly source rocks become the main sources of the accumulated condensate gas in the study area. This finding enables prospective exploration areas to be delineated according to the spatial distribution of the Jurassic sources.

Author Contributions: Conceptualization, X.W., K.L., J.L. and L.Z.; Data curation, X.W., L.Z. and X.D.; Formal analysis, X.W. and K.L.; Funding acquisition, K.L., X.Y., J.L., L.Z. and X.D.; Investigation, X.W. and X.D.; Methodology, X.W., K.L. and J.L.; Project administration, X.Y. and L.Z.; Resources, K.L. and X.Y.; Software, J.L.; Supervision, K.L.; Validation, X.W., K.L., X.Y. and X.D.; Visualization, J.L.; Writing—original draft, X.W.; Writing—review and editing, K.L. All authors have read and agreed to the published version of the manuscript.

Funding: This research was funded by the Major Research Project on the Tethys Geodynamic System of the National Natural Science Foundation of China (No. 92055204), NSFC Innovation Group (No. 41821002), and PetroChina Major Research Program on Deep Petroleum System in the Tarim Basin (No. ZD2019-183-01-004). The Tarim Oilfield Company, PetroChina is thanked for providing their inhouse data used in this paper.

Institutional Review Board Statement: Not applicable.

Informed Consent Statement: Not applicable.

Data Availability Statement: The data presented in this study are available on request from the corresponding author. The data are not publicly available due to privacy.

Conflicts of Interest: Author Xianzhang Yang and Lu Zhou were employed by the PetroChina Tarim Oilfield Company. The remaining authors declare that the research was conducted in the absence of any commercial or financial relationships that could be construed as a potential conflict of interest.

References

1. Morley, C.K.; King, R.; Hillis, R.; Tingay, M.; Backe, G. Deepwater fold and thrust belt classification, tectonics, structure and hydrocarbon prospectivity: A review. *Earth-Sci. Rev.* **2001**, *104*, 41–91. [CrossRef]
2. Zelilidis, A.; Maravelis, A.G.; Tserolas, P.; Konstantopoulos, P.A. An overview of the petroleum systems in the Ionian Zone onshore NW Greece and Albania. *J. Pet. Geol.* **2015**, *38*, 331–348. [CrossRef]
3. Obermayer, M.; Osadetz, K.G.; Fowler, M.G.; Snowdon, L.R. Light hydrocarbon (gasoline range) parameter refinement of biomarker-based oil–oil correlation studies: An example from Williston Basin. *Org. Geochem.* **2000**, *31*, 959–976. [CrossRef]
4. Bailey, N.J.; Burwood, R.; Harriman, G.E. Application of pyrolysate carbon isotope and biomarker technology to organofacies definition and oil correlation problems in North Sea basins. *Org. Geochem.* **1990**, *16*, 1157–1172. [CrossRef]
5. Curiale, J.A. High-resolution organic record of Bridge Creek deposition, northwest New Mexico. *Org. Geochem.* **1994**, *21*, 489–507. [CrossRef]
6. Requejo, A.G. Maturation of petroleum source rocks—II. Quantitative changes in extractable hydrocarbon content and composition associated with hydrocarbon generation. *Org. Geochem.* **1994**, *21*, 91–105. [CrossRef]
7. Dzou, L.I.P.; Noble, R.A.; Senftle, J.T. Maturation effects on absolute biomarker concentration in a suite of coals and associated vitrinite concentrates. *Org. Geochem.* **1995**, *23*, 681–697. [CrossRef]
8. Farrimond, P.; Taylor, A.; TelnÆs, N. Biomarker maturity parameters: The role of generation and thermal degradation. *Org. Geochem.* **1998**, *29*, 1181–1197. [CrossRef]
9. Fang, R.; Littke, R.; Zieger, L.; Baniasad, A.; Li, M.; Schwarzbauer, J. Changes of composition and content of tricyclic terpane, hopane, sterane, and aromatic biomarkers throughout the oil window: A detailed study on maturity parameters of Lower Toarcian Posidonia Shale of the Hils Syncline, NW Germany. *Org. Geochem.* **2019**, *138*, 103928. [CrossRef]
10. Hakimi, M.H.; Alaug, A.S.; Kahal, A.Y.; Rahim, A.; Radwan, A.E.; Talha Qadri, S.M. Organic matter characteristics and gas generation prospect of the fluvial deltaic organic-rich shale in the offshore Jiza-Qamar Basin, Yemen, based on organic geochemical, macerals composition, and biomarker results combined with 1-D basin modeling. *Geol. J.* **2023**, *58*, 4035–4056. [CrossRef]
11. Moldowan, J.M.; Sundararamun, P.; Schoell, M. Sensitivity of biomarker properties to deposition environment and/or source input in the Lower Toarcian of S. W. Germany. *Org. Geochem.* **1986**, *10*, 915–926. [CrossRef]
12. Keller, M.A.; Macquaker, J.H.S. High resolution analysis of petroleum source potential and lithofacies of Lower Cretaceous mudstone core (Pebble Shale Unit and GRZ of Hue Shale), Mikkelsen Bay State #1 Well, North Slope Alaska. In *Petroleum Plays and Systems in the National Petroleum Reserve-Alaska*; Houseknecht, D.W., Ed.; Society of Economic Paleontologists and Mineralogists, SEPM Core Workshop: Tulsa, OK, USA, 2001; Volume 21, pp. 37–56.
13. Barker, C.E.; Pawlewicz, M.; Cobabe, E.A. Deposition of sedimentary organic matter in black shale facies indicated by the geochemistry and petrography of high-resolution samples, Blake Nose, western North Atlantic. In *Western North Atlantic Palaeogene and Cretaceous Palaeoceanography*; Geological Society: London, UK, 2001; Volume 183, pp. 49–72.
14. Curiale, J.A. Oil–source rock correlations—Limitations and recommendations. *Org. Geochem.* **2008**, *39*, 1150–1161. [CrossRef]
15. Hunt, J.M. *Petroleum Geochemistry and Geology*; W H Freemme and Company: San Francisco, CA, USA, 1979; pp. 25–189.
16. Rullkötter, J. Gas chromatography/mass spectrometry of degraded triterpanes in fossil organic matter—A record of microbial action. *Int. J. Mass Spectrom.* **1983**, *48*, 39–42. [CrossRef]
17. Peters, K.E.; Walters, C.C.; Moldowan, J.M. *The Biomarker Guide: Biomarkers and Isotopes in Petroleum Exploration and Earth History*; Cambridge University: London, UK, 2005; Volume 2, pp. 511–559.
18. Waples, D.W.; Curiale, J.A. Oil–oil and oil–source rock correlations. In *Exploring for Oil and Gas Traps*; Beaumont, E.A., Foster, N.H., Eds.; American Association of Petroleum Geology: Tulsa, OK, USA, 1999; Chapter 8; pp. 1–71.
19. Maravelis, A.G.; Koukounya, A.; Tserolas, P.; Pasadakis, N.; Zelilidis, A. Geochemistry of Upper Miocene-Lower Pliocene source rocks in the Hellenic Fold and Thrust Belt, Zakynthos Island, Ionian Sea, western Greece. *Mar. Pet. Geol.* **2015**, *66*, 217–230. [CrossRef]
20. George, S.C.; Krieger, F.W.; Eadington, P.J.; Quezada, R.A.; Greenwood, P.F.; Eisenberg, L.I.; Hamilton, P.J.; Wilson, M.A. Geochemical comparison of oil-bearing fluid inclusions and produced oil from the Toro sandstone, Papua New Guinea. *Org. Geochem.* **1997**, *26*, 155–173. [CrossRef]
21. Bourdet, J.; Eadington, P.; Volk, H.; George, S.C.; Pironon, J.; Kempton, R. Chemical changes of fluid inclusion oil trapped during the evolution of an oil reservoir: Jabiru–1A case study (Timor Sea, Australia). *Mar. Pet. Geol.* **2012**, *36*, 118–139. [CrossRef]
22. Karlsen, D.A.; Nedkvitne, T.; Larter, S.R.; Bjørlykke, K. Hydrocarbon composition of authigenic inclusions: Application to elucidation of petroleum reservoir filling history. *Geochim. Cosmochim. Acta* **1993**, *57*, 3641–3659. [CrossRef]

23. Pan, C.; Yang, J.; Fu, J.; Sheng, G. Molecular correlation of free oil and inclusion oil of reservoir rocks in the Junggar Basin, China. *Org. Geochem.* **2003**, *34*, 357–374. [CrossRef]
24. Volk, H.; George, S.C.; Middleton, H.; Schofield, S. Geochemical comparison of fluid inclusion and present-day oil accumulations in the Papuan Foreland—Evidence for previously unrecognised petroleum source rocks. *Org. Geochem.* **2005**, *36*, 29–51. [CrossRef]
25. Volk, H.; George, S.C.; Killops, S.D.; Lisk, M.; Ahmed, M.; Quezada, R.A. The use of fluid inclusion oils to reconstruct the charge history of petroleum reservoirs—An example from the Taranaki Basin. In Proceedings of the 2002 New Zealand Petroleum Conference: Crown Minerals, Auckland, New Zealand, 24–27 February 2002; pp. 221–233.
26. Hagemann, H.W.; Hollerbach, A. The fluorescence behaviour of crude oils with respect to their thermal maturation and degradation. *Org. Geochem.* **1986**, *10*, 473–480. [CrossRef]
27. Stasiuk, L.D.; Snowdon, L.R. Fluorescence micro-spectrometry of synthetic and natural hydrocarbon fluid inclusions: Crude oil chemistry, density and application to petroleum migration. *Appl. Geochem.* **1997**, *12*, 229–241. [CrossRef]
28. Chang, Y.; Huang, W. Simulation of the fluorescence evolution of "live" oils from kerogens in a diamond anvil cell: Application to inclusion oils in terms of maturity and source. *Geochim. Cosmochim. Acta* **2008**, *72*, 3771–3787. [CrossRef]
29. Macleod, G.; Petch, G.S.; Larter, S.R.; Aplin, A.C. Investigations of the composition of hydrocarbon fluid inclusions. In Proceeding of the 205th ACS National Meeting, Division of Geochemistry, Denver, FL, USA, 28 March–2 April 1993.
30. Cheng, K.; Xiong, Y.; Zeng, X. Research on coal-derived hydrocarbon in Turpan-Hami Basin. *Acta Pet. Sin.* **2002**, *23*, 13–17.
31. Xiong, Y.; Cheng, K.; Yang, Z. Advances in the correlation of oils and source in the Jiuxi depression, Northwest China. *Pet. Explor. Dev.* **2004**, *31*, 36–39.
32. Leo, C.O.; Nicolas, C.O.; Mudiaga, C.O. Multivariate analysis of source and maturity biomarker indices of crude oils from SW Niger Delta. *J. Geoscil.* **2014**, *18*, 365–371.
33. Irwin, H.; Meyer, T. Lacustrine organic facies. A biomarker study using multivariate statistical analysis. *Org. Geochem.* **1990**, *16*, 197–210. [CrossRef]
34. Peters, K.E.; Moldowan, J.M.; Schoell, M.; Hempkins, W.B. Petroleum isotopic and biomarker composition related to source rock organic matter and depositional environment. *Org. Geochem.* **1986**, *10*, 17–27. [CrossRef]
35. Zumberge, H.E. Prediction of source rock characteristics based on terpane biomarkers in crude oils: A multivariate statistical approach. *Geochim. Cosmochim. Acta* **1987**, *51*, 1625–1637. [CrossRef]
36. Welte, D.H.; Yalcin, M.N. Basin modelling- A new comprehensive methodology in petroleum geology. *Org. Geochem.* **1988**, *13*, 141–151. [CrossRef]
37. Poelchau, H.S.; Baker, D.R.; Hantschel, T.; Horsfield, B.; Wygrala, B. Basin simulation and the design of the conceptual basin model. In *Petroleum and Basin Evolution*; Welte, D.H., Horsfield, B., Baker, D.R., Eds.; Springer: Berlin, Germany, 1997; pp. 5–70.
38. Burgreen-Chan, B.; Graham, S.A. Petroleum system modeling of the East Coast Basin, Hawke Bay, New Zealand. *AAPG Bull.* **2018**, *102*, 587–612. [CrossRef]
39. D' Ambrosio, A.; Lipparini, L.; Bigi, S.; Cassola, T.; Bambridge, V.R.; Derks, J.F.; Trippetta, F. Structural restoration and basin modelling of the central apennine orogen/fordeep/foreland system: New insights on the regional petroleum system. *Mar. Petr. Geol.* **2021**, *127*, 104948. [CrossRef]
40. Underdown, R.; Redfern, J. Petroleum generation and migration in the Ghadames Basin, North Africa: A two-dimensional basin-modeling study. *AAPG Bull.* **2008**, *92*, 53–76. [CrossRef]
41. Hakimi, M.H.; Najaf, A.A.; Abdula, R.A.; Mohialdeen, I.M.J. Generation and expulsion history of oil-source rock (Middle Jurassic Sargelu Formation) in the Kurdistan of north Iraq, Zagros folded belt: Implications from 1D basin modeling study. *J. Pet. Sci. Eng.* **2017**, *162*, 852–872. [CrossRef]
42. Pang, X.; Peng, J.; Jiang, Z.; Yang, H.; Wang, P.; Jiang, F.; Wang, K. Hydrocarbon accumulation processes and mechanisms in Lower Jurassic tight sandstone reservoirs in the Kuqa subbasin, Tarim Basin, northwest China: A case study of the Dibei tight gas field. *AAPG Bull.* **2019**, *4*, 769–796. [CrossRef]
43. Jia, C.; Li, Q. Petroleum geology of Kela-2, the most productive gas field in China. *Mar. Pet. Geol.* **2008**, *25*, 335–343.
44. Li, J.; Wang, C.; Li, J.; Ma, W.; Zhang, H.; Lu, Y.; Li, D.; Liu, M. Source and exploration direction of tight oil and gas in the Dibei section of northern Kuqa depression. *China Pet. Explor.* **2019**, *24*, 485–497. (In Chinese with English abstract)
45. Tang, Y.; Yang, X.; Xie, H.; Xu, Z.; Wei, H.; Xie, Y. Tight gas reservoir characteristics and exploration potential of jurassic Ahe Formation in Kuqa depression, Tarim Basin. *China Pet. Explor.* **2021**, *26*, 113–124. (In Chinese with English abstract)
46. Wang, Q.; Zhang, R.; Yang, X.; Yu, Z.; Xu, Z.; Zhou, L.; Wang, K.; Zhang, L. Major breakthrough and geological significance of tight sandstones gsa exploration in Jurassic Ahe Formation in Dibei area, eastern Kuqa depression. *Acta Pet. Sin.* **2022**, *43*, 1050–1064. (In Chinese with English abstract)
47. Hanson, A.D.; Zhang, S.C.; Moldowan, J.M.; Liang, D.G.; Zhang, B.M. Molecular organic geochemistry of the Tarim Basin, Northwest China. *AAPG Bull.* **2000**, *84*, 1109–1128.
48. Liang, D.; Zhang, S.; Chen, J.; Wang, F.; Wang, P. Organic geochemistry of oil and gas in the Kuqa depression, Tarim Basin, NW China. *Org. Geochem.* **2003**, *34*, 873–888. [CrossRef]

49. Qin, S.; Dai, J.; Liu, X. The controlling factors of oil and gas generation from coal in the Kuqa Depression of Tarim Basin, China. *Int. J. Coal Geol.* **2007**, *70*, 255–263. [CrossRef]
50. Shi, G.; Zhang, Q.; Yang, X.; Mi, S. Oil and gas assessment of the Kuqa Depression of Tarim Basin in western China: By simple fluid flow models of primary and secondary migrations of hydrocarbons. *J. Pet. Sci. Eng.* **2010**, *75*, 77–90. [CrossRef]
51. Jiang, H.; Pang, X.; Yu, R.; Chen, D.; Zhao, J.; Hu, T. Lower limit of hydrocarbon accumulation in the Kuqa Depression, Tarim Basin, NW China. *Geol. J.* **2017**, *52*, 141–153. [CrossRef]
52. Song, X.; Lyu, X.; Shen, Y.; Guo, S. Hydrocarbon migration and accumulation history in deep reservoirs: A case study of Mesozoic sandstone gas reservoirs in the Kelasu-Yiqikelike structural belt of the Kuqa Depression, Tarim Basin. *J. Geosci.* **2019**, *23*, 69–86. [CrossRef]
53. Wu, H.; Yan, S.; Zhao, M.; Lu, X. Hydrocarbon accumulation prospect and charge history of the northern monocline belt in Kuqa Depression of Tarim Basin, western China. *Nat. Gas Geosci.* **2015**, *26*, 2325–2335. (In Chinese with English abstract)
54. Graham, S.A.; Hendrix, M.S.; Wang, L.B.; Carroll, A.R. Collision successor basins of western China, impact of tectonic inheritance on sand composition. *GSA Bull.* **1993**, *105*, 323–344. [CrossRef]
55. Wei, G.; Zhang, R.; Zhi, F.; Wang, K.; Yu, C.; Dong, C. Formation conditions and exploration directions of Mesozoic structural-lithologic reservoirs in the eastern Kuqa depression. *Acta Pet. Sin.* **2021**, *42*, 1113–1125.
56. Zou, C.; Jia, J.; Tao, S.; Tao, X. Analysis of Reservoirs Forming Conditions and Prediction of Continuous Tight Gas Reservoirs for the Deep Jurassic in the Eastern Kuqa Depression, Tarim Basin. *Acta Geol. Sin.* **2011**, *85*, 1173–1186. [CrossRef]
57. Ju, W.; Hou, G.; Huang, S.; Ren, K. Structural fracture distribution and prediction of the lower Jurassic Ahe Formation sandstone in the Yinan-Tuzi area, Kuqa depression. *Geotecton. Metallog.* **2013**, *37*, 592–602.
58. Lu, H.; Lu, X.; Fan, J.; Zhao, M.; Wei, H.; Zhang, B.; Lu, Y. Controlling effect of fractures on gas accumulation and production within the tight sandstone: A case study on the Jurassic Dibei gas reservoir in the eastern part of the Kuqa foreland basin, China. *Nat. Gas Geosci.* **2016**, *1*, 61–71. [CrossRef]
59. Wang, H.; Wu, T.; Fu, X.; Liu, B.; Wang, S.; Jia, R.; Zhang, C. Quantitative determination of the brittle–ductile transition characteristics of caprocks and its geological significance in the Kuqa depression, Tarim Basin, western China. *J. Pet. Sci. Eng.* **2019**, *173*, 492–500. [CrossRef]
60. Molnar, P.; Tapponnier, P. Cenozoic Tectonics of Asia: Effects of a Continental Collision: Features of recent continental tectonics in Asia can be interpreted as results of the India-Eurasia collision. *Science* **1975**, *189*, 419–426. [CrossRef] [PubMed]
61. Du, J.; Wang, Z.; Hu, S.; Wang, Q.; Xie, H. Formation conditions and geological characteristics of deep giant gas provinces in the Kuqa foreland thrust belt. *Pet. Explor. Dev.* **2012**, *39*, 413–422. [CrossRef]
62. Guo, S.; Lyu, X.; Zhang, Y. Relationship between tight sandstone reservoir formation and hydrocarbon charging: A case study of a Jurassic reservoir in the eastern Kuqa Depression, Tarim Basin, NW China. *J. Nat. Gas Sci. Eng.* **2018**, *52*, 304–316. [CrossRef]
63. Liu, J.; Jiang, Z.; Liu, K.; Gui, L.; Xing, J. Hydrocarbon sources and charge history in the Southern Slope Region, Kuqa Foreland Basin, northwestern China. *Mar. Pet. Geol.* **2016**, *74*, 26–46. [CrossRef]
64. Lisk, M.; Eadington, P.J. Oil migration in the Cartier Through, Vulcan Sub–basin. In *The Sedimentary Basins of WA: Proceedings PESA Symposium, Perth, Australia*; Purcell, P.G., Purcell, R.R., Eds.; Petroleum Exploration Society of Australia (PESA): Perth, Australia, 1994; pp. 301–312.
65. O'Brien, G.W.; Lisk, M.; Duddy, I.; Eadington, P.J.; Cadman, S.; Fellows, M. Late Tertiary fluid migration in the Timor Sea: A key control on thermal and diagenetic histories. *APPEA* **1996**, *36*, 399–427. [CrossRef]
66. Eadington, P.J.; Kempton, R.H. New developments to investigate models of oil accumulation and fluid interactions in reservoirs using data from fluid inclusions. In Proceeding of the APPEA Conference & Exhibition, Perth, Australia, 6–9 April 2008; Volume 48.
67. Liu, K.; George, S.C.; Lu, X.; Gong, S.; Tian, H.; Gui, L. Innovative fluorescence spectrophotometric techniques for rapidly characterizing oil inclusions. *Org. Geochem.* **2014**, *72*, 34–45. [CrossRef]
68. George, S.C.; Volk, H.; Dutkiewicz, A. Mass spectrometry techniques for analysis of oil and gas trapped in fluid inclusions. In *Mass Spectrometry Handbook*; Lee, M.S., Ed.; John Wiley & Sons, Inc.: Hoboken, NJ, USA, 2012; pp. 645–673.
69. Pradhan, U.K.; Shirodkar, P.V.; Shahu, B.K. Physicochemical characteristic of the coastal water off Devi estuary, Orissa and evaluation of its seasonal changes using chemometric techniques. *Curr. Sci.* **2009**, *96*, 1203–1209.
70. Onojake, M.C.; Ukerun, S.O.; Iwuoha, G. A Statistical Approach for Evaluation of the Effects of Industrial and Municipal Wastes on Warri Rivers, Niger Delta, Nigeria. *Water Qual. Expo. Health* **2011**, *3*, 91–99. [CrossRef]
71. Odden, W.; Kvalheim, O.M. Application of multivariate modeling to detect hydrocarbon components for optimal discrimination between two source rock types. *Appl. Geochem.* **2000**, *15*, 611–627. [CrossRef]
72. Elliott, D. The construction of balanced cross-section. *J. Struct. Geol.* **1983**, *5*, 101. [CrossRef]
73. Dahlstrom, C.D.A. Balanced cross sections. *Can. J. Earth Sci.* **1969**, *6*, 743–757. [CrossRef]
74. Dennison, J.M.; Woodward, H.P. Palinspastic maps of central Appalachians. *AAPG Bull.* **1963**, *47*, 666–680.

75. Maerten, L.; Gillespie, P.; Daniel, J.-M. 3-D geomechanical modeling for constraint of subseismic fault simulation. *AAPG Bull.* **2006**, *90*, 1337–1358. [CrossRef]
76. Suppe, J.; Donald, A. Medwedeff Geometry and kinematics of fault-propagation folding. *Eclogae Geol. Helv.* **1983**, *283*, 684–721.
77. Williams, G.; Chapman, T. Strains developed in the hanging walls of trusts due to their slip-propagation rate, a dislocation model. *J. Struct. Geol.* **1983**, *5*, 563–571. [CrossRef]
78. Waples, D.W.; Suizu, M.; Kamata, H. The art of maturity modeling: Part 2—-Alternative models and sensitivity analysis. *AAPG Bull.* **1992**, *76*, 47–66.
79. Pepper, A.S.; Corvi, P.J. Simple kinetic models of petroleum formation: Part I—Oil and gas generation from kerogen. *Mar. Pet. Geol.* **1995**, *12*, 291–319. [CrossRef]
80. Tissot, B.P.; Pelet, R.; Ungerer, P. Thermal history of sedimentary basins, maturation indices, and kinetics of oil and gas generation. *AAPG Bull.* **1987**, *71*, 1445–1466.
81. Peters, K.E.; Burnham, A.K.; Walters, C.C. Petroleum generation kinetics: Single versus multiple heating-ramp open-system pyrolysis. *AAPG Bull.* **2015**, *99*, 591–616. [CrossRef]
82. Ungerer, P.; Burrus, J.; Doligez, B.; Chenet, P.Y.; Bessis, F. Basin evaluation by integrated two-dimensional modelling of heat transfer, fluid flow, hydrocarbon generation, and migration. *AAPG Bull.* **1990**, *74*, 309–334.
83. Dieckmann, V. Modelling petroleum formation from heterogeneous source rocks: The influence of frequency factors on activation energy distribution and geological prediction. *Mar. Pet. Geol.* **2005**, *22*, 375–390. [CrossRef]
84. Liu, J.; Yang, X.; Liu, K.; Xu, Z.; Jia, K.; Lu, Z.; Wei, H.; Zhang, L.; Wu, S.; Wei, X. Differential hydrocarbon generation and evolution of typical terrestrial gas-prone source rocks: An example from the Kuqa foreland basin, NW China. *Mar. Pet. Geol.* **2023**, *152*, 106225. [CrossRef]
85. Cheng, K.; Wang, Z. Hydrocarbon generation condition study for marine carbonate in high-mature and over-mature stage. *Sci. China Earth Sci.* **1996**, *26*, 537–543. (In Chinese)
86. Cheng, K.; Wang, Z.; Xiong, Y.; Zhong, N. Hydrocarbon generation research for marine carbonate in China. *Mar. Origin Pet. Geol.* **1999**, *4*, 1–11. (In Chinese)
87. Lu, S.; Xue, H.; Zhong, N. Simulating Calculation of the Variations of Organic Matter Abundance and Hydrocarbon-generating Potential during Geological Process. *Geol. Rev.* **2003**, *49*, 292–297. (In Chinese with English abstract)
88. Wygrala, B.P. *Integrated Study of an Oil Field in the Southern Po Basin, Northern Italy*; Forschungszentrum Karlsruhe/Jülich: Karlsruhe, Germany; Jülich, Germany, 1989; p. 217.
89. Guo, Y.; Pang, X.; Dong, Y.; Jiang, Z.; Chen, D.; Jiang, F. Hydrocarbon generation and migration in the Nanpu Sag, Bohai Bay Basin, eastern China: Insight from basin and petroleum system modeling. *J. Asian Earth Sci.* **2013**, *77*, 140–150. [CrossRef]
90. Deng, L.; Wang, Y. Dynamic simulation approach to the evolution history of the palaeotemperature field of a basin. *J. Chengdu Univ. Technol.* **1998**, *25*, 38–47. (In Chinese with English abstract)
91. Wang, L.; Li, C.; Liu, S.; Li, H.; Xu, M.; Yu, D.; Jia, C.; Wei, G. Terrestrial heatflow distribution in Kuqa foreland basin, Tatrim Basin, NW China. *Pet. Explor. Dev.* **2005**, *32*, 79–84. (In Chinese with English abstract)
92. Qiu, N.; Chang, J.; Feng, Q.; Zeng, S.; Liu, X.; Li, H.; Ma, A. Maturity evolution of deep and ultra-deep source rocks in the Chinese central and western basins. *Earth Sci. Front.* **2023**, *30*, 199–212. (In Chinese with English abstract)
93. Kvalheim, O.M.; Christy, A.A.; Telnæs, N.; Bjørseth, A. Maturity determination of organic matter in coals using the methylphenanthrene distribution. *Geochim. Cosmochim. Acta* **1987**, *51*, 1883–1888. [CrossRef]
94. Gao, T.; Ding, X.; Yang, X.; Chen, C.; Xu, Z.; Liu, K.; Zhang, X.; Cao, W. Geochemical Characteristics and Depositional Environment of Coal-Measure Hydrocarbon Source Rocks in the Northern Tectonic Belt, Kuqa Depression. *Appl. Sci.* **2022**, *12*, 9464. [CrossRef]
95. Didyk, B.M.; Simoneit, B.R.T.; Brassell, S.C.; Eglinton, G. Organic geochemical indicators of palaeoenvironmental conditions of sedimentation. *Nature* **1978**, *272*, 216–222. [CrossRef]
96. Philp, R.P.; Gilbert, T.D. Source rock and asphaltene biomarker characterization by pyrolysisgas chromatography-mass spectrometry-multiple ion detection. *Geochim. Cosmochim. Acta* **1985**, *49*, 1421–1432. [CrossRef]
97. Boudou, J.-P.; Pelet, R.; Letolle, R. A model of the diagenetic evolution of coaly sedimentary organic matter. *Geochim. Cosmochim. Acta* **1984**, *48*, 1357–1362. [CrossRef]
98. Koopmans, M.P.; Koster, J.; Kaam–Peters, H.M.E.; Kenig, F.; Schouten, S.; Hartger, W.; Leeuw, J.W. Diagenetic and Catagenetia products of isorenieratene: Molecular indicators for photic zone anoxia. *Geochim. Cosmochim. Acta* **1996**, *60*, 67–96. [CrossRef]
99. Huang, W.; Meinschein, W.G. Sterols as ecological indicators. *Geochim. Cosmochim. Acta* **1979**, *43*, 739–745. [CrossRef]
100. He, T.; Lu, S.; Li, W.; Wang, W.; Sun, D.; Pan, W.; Zhang, B. Geochemical characteristics and effectiveness of thick, black shales in southwestern depression, Tarim Basin. *J. Pet. Sci. Eng.* **2019**, *185*, 106607. [CrossRef]
101. Kleemann, D.O.; Walker, S.K.; Walkley, J.R.W.; Smith, D.H.; Ponzoni, R.W.; Seamark, R.F. Factors influencing lamb survival in a high fecundity Booroola Merino × South Australian Merino flock. *Theriogenology* **1990**, *33*, 965–976. [CrossRef]
102. Damsté, J.S.S.; Leeuw, J.W.D. Analysis, structure and geochemical significance of organically -bound sulphur in the geosphere: State of the art and future research. *Org. Geochem.* **1990**, *16*, 1077–1101. [CrossRef]

103. Moldowan, J.M.; Seifert, W.K.; Gallegos, E.J. Relationship between petroleum composition and depositional environment of petroleum source rocks. *AAPG Bull.* **1985**, *69*, 1255–1268.
104. Cheng, B.; Liu, H.; Cao, Z.; Wu, X.; Chen, Z. Origin of deep oil accumulations in carbonate reservoirs within the north Tarim Basin: Insights from molecular and isotopic compositions. *Org. Geochem.* **2020**, *139*, 103931. [CrossRef]
105. Radke, M.; Willsch, H.; Leythaeuser, D.; Teichmüller, M. Aromatic components of coal: Relation of distribution pattern to rank. *Geochim. Cosmochim. Acta* **1982**, *46*, 1831–1848. [CrossRef]
106. Hou, D.; Xiao, Z.; Tang, Y.; Zhu, J.; Li, X. Geochemical characterization of mixing natural gas in Kekeya Field, Tarim Basin, China. *Nat. Gas Geosci.* **2003**, *14*, 474–479. (In Chinese with English abstract)
107. Zhang, M.; Huang, G.; Zhao, H.; Wang, X. Genetic features of gas-condensate reservoirs in the Kekeya Field, southwest depression in the Tarim Basin, China. *Sci. China Earth Sci.* **2008**, *52*, 19–25. (In Chinese with English abstract) [CrossRef]
108. Li, J.; Xie, Z.; Li, Z.; Luo, X.; Ju, G.; Gong, S. A gas source study for Kuqa depression. *Pet. Explor. Dev.* **2001**, *28*, 29–41.
109. Li, J.; Hao, A.; Qi, X.; Chen, X.; Guo, J.; Ran, Q.; Li, Z.; Xie, Z.; Zeng, X.; Li, J.; et al. Geochemical characteristics and exploration potential of Jurassic coal-formed gas in northwest China. *Nat. Gas Geosci.* **2019**, *4*, 321–335. [CrossRef]
110. Zou, Y.; Zhao, C.; Wang, Y.; Zhao, W.; Peng, P.; Shuai, Y. Characteristics and origin of natural gases in the Kuqa Depression of Tarim Basin, NW China. *Org. Geochem.* **2006**, *37*, 280–290. [CrossRef]

Disclaimer/Publisher's Note: The statements, opinions and data contained in all publications are solely those of the individual author(s) and contributor(s) and not of MDPI and/or the editor(s). MDPI and/or the editor(s) disclaim responsibility for any injury to people or property resulting from any ideas, methods, instructions or products referred to in the content.